



1 Laser ablation aerosol particle time-of-flight mass spectrometer 2 (LAAPTOF): Performance, reference spectra and classification of 3 atmospheric samples

4 Xiaoli Shen^{1,2}, Ramakrishna Ramisetty¹, Claudia Mohr^{1,3}, Wei Huang^{1,2}, Thomas Leisner¹, Harald
5 Saathoff^{1,*}

6 ¹Institute of Meteorology and Climate Research (IMK-AAF), Karlsruhe Institute of Technology (KIT), Hermann-von-
7 Helmholtz-Platz 1, 76344 Eggenstein-Leopoldshafen, Germany

8 ²Institute of Geography and Geoecology (IfGG), Karlsruhe Institute of Technology (KIT), Kaiserstr.12, 76131 Karlsruhe,
9 Germany

10 ³Now at: Department of Environmental Science and Analytical Chemistry, Stockholm University, Stockholm, 11418, Sweden

11 *Correspondence to: Harald Saathoff (harald.saathoff@kit.edu)

12 **Abstract.** The laser ablation aerosol particles time-of-flight mass spectrometer (LAAPTOF, Aeromegt GmbH) is able to identify
13 the chemical composition and mixing state of individual aerosol particles, and thus is a tool for elucidating their impacts on
14 human health, visibility, ecosystem and climate. The overall detection efficiency (ODE) of the instrument we use was
15 determined to range from $\sim(0.01 \pm 0.01)\%$ to $\sim(6.57 \pm 2.38)\%$ for polystyrene latex (PSL), ammonium nitrate (NH_4NO_3), and
16 sodium chloride (NaCl) particles in the size range of 200 to 2000 nm. Reference mass spectra of 32 different particle types
17 relevant for atmospheric aerosol (e.g. pure compounds NH_4NO_3 , K_2SO_4 , NaCl, oxalic acid, pinic acid, and pinonic acid; internal
18 mixtures of e.g. salts, secondary organic aerosol, and metallic core-organic shell particles; more complex particles such as soot
19 and dust particles) were determined. Our results show that internally mixed aerosol particles can result in spectra with new
20 clusters of ions, rather than simply a combination of the spectra from the single components. An exemplary one-day ambient
21 data set was analysed by classical Fuzzy-clustering leading to six different particle classes. Correlating these particle classes with
22 the reference spectra as well as direct comparison of the ambient data with the reference spectra has proven how useful they are
23 for the interpretation of field measurements, for e.g. grouping data, and identifying special particle types and potential sources.

24

25 1 Introduction

26 Atmospheric aerosol particles impact visibility, interact with trace gases, can act as cloud condensation and ice nuclei, and
27 influence the Earth's radiation budget (Seinfeld and Pandis, 2006). Especially the continuously evolving chemical composition
28 of aerosol particles is of scientific interest, as it influences all aerosol effects (Burkholder et al., 2017; Pöschl, 2005). However,
29 large knowledge gaps still exist related to the chemical composition of the organic and inorganic components and their mutual
30 interaction (Jimenez et al., 2009; Murphy et al., 2006; Schill and Tolbert, 2013; Zhang et al., 2007).

31 Aerosol particles can contain various components ranging from volatile (e.g. nitrate, sulphate, ammonium salts, and many
32 organic compounds), to refractory species (e.g. elemental carbon, minerals, and sea salt) (Pratt and Prather, 2012). The global
33 aerosol mass burden was estimated to consist of 73.6% dust, 16.7% sea salt, 2.8% biogenic secondary organic aerosols (SOA),
34 2.3% primary organic aerosols (POA), 1.3% sulphate, 1.3% ammonium, 1.2% nitrate, 0.4% black carbon (soot), 0.2%
35 anthropogenic SOA, and 0.2% methane sulphonic acid (Tsigaridis et al., 2006). SOA is estimated to account for the major



36 fraction of the total organic aerosol mass with dicarboxylic acids, such as oxalic acid suggested to be the main contributors
37 (Ervens et al., 2004). Ambient aerosols, either directly emitted (primary aerosols) or formed in the atmosphere (secondary
38 aerosols) from oxidation of gas-phase precursors or chemical reactions on particles, have typical lifetimes ranging from hours to
39 a few weeks (Pöschl, 2005). During their lifetime, the complexity of their chemical composition usually increases by coagulation,
40 cloud processing, or chemical reactions: Sea salt, POA, soot, or dust particles can e.g. heterogeneously react with secondary
41 organic compounds like organic acids and secondary inorganic compounds like sulfuric or nitric acid (Seinfeld and Pandis, 2006;
42 Usher et al., 2003). This modifies the particles' mixing state, with both internal (individual particles consisting of mixed
43 compounds, e.g. coating structures) and external mixtures (e.g. mixture of particles consisting of different compounds) (Li et al.,
44 2016). This underscores the importance of measuring aerosol chemical composition and its changes on short timescales and on a
45 single particle basis, which can be realized by on-line mass spectrometry.

46 One-line mass spectrometry includes bulk and single-particle measurements (Pratt and Prather, 2012). Single particle mass
47 spectrometry, which can be dated back to the 1970s, aims at in situ and real time identification of the chemical composition of
48 individual aerosol particles, hereby elucidating a particle's external and internal mixing properties (Noble and Prather, 2000).
49 Online single particle mass spectrometers (SPMS) commonly use pulsed lasers for particle desorption and ionization (LDI), with
50 the advantage of ionizing nearly all atmospheric particle components, including both non-refractory and refractory materials
51 (Kulkarni et al., 2011). To the best of our knowledge, so far no SPMS analysis is yet capable of providing a quantitative
52 composition analysis, since the ablation/ionization laser cannot interact with the entire particle, and the resulting ion fragments
53 and clusters are susceptible to matrix effects. In addition, ionization mechanisms are not fully understood (Murphy, 2007). The
54 first commercial SPMS combined LDI with a Time-of-Flight Mass Spectrometer (aerosol time-of-flight mass spectrometer,
55 ATOFMS, TSI GmbH) (Gard et al., 1997; Su et al., 2004). Several other home-build research SPMS were developed, each with
56 different advantages: Particle Analysis by Laser Mass Spectrometry (PALMS) (Murphy, 2007; Murphy and Thomson, 1995),
57 Laser Mass Analyser for Particles in the Airborne State (LAMPAS) (Trimborn et al., 2000), Single Particle Analysis and Sizing
58 System (SPASS) (Erdmann et al., 2005), Single Particle Laser Ablation Time-of-Flight Mass Spectrometer (SPLAT) (Zelenyuk
59 and Imre, 2005; Zelenyuk et al., 2009), Aircraft-based Laser Ablation Aerosol Mass spectrometer (ALABAMA) (Brands et al.,
60 2011), and Single Particle Laser Ablation Mass Spectrometer (SPLAM) (Gaie-Levrel et al., 2012) to name some of them. SPMS
61 have identified many different ambient particle types in different regions of the atmosphere, such as an elemental carbon/organic
62 carbon (ECOC), organic-sulphate, aged sea salt, biological, soil dust, and different metal dominated types (Dall'Osto et al., 2016;
63 Moffet et al., 2008; Murphy et al., 2006; Schmidt et al., 2017). These measurements all confirmed the complexity of individual
64 particles' mixing state, and demonstrated the usefulness of single particle mass spectra for apportionment of individual particle
65 sources, including e.g. fossil fuel and biomass burning combustion, cooking, marine, and shipping sources (Arndt et al., 2016;
66 Schmidt et al., 2017).

67 Currently, the only commercially available SPMS is the Laser Ablation Aerosol Particles Time-of-Flight mass spectrometer
68 (LAAPTOF, Aeromegt GmbH). It uses two laser diodes (wave length 405 nm, ~40 mW, ~50 µm beam spot diameter) for optical
69 counting and size recording by light scattering, and one excimer laser (ArF, 193 nm, ~4 mJ) for one step ablation/ionization.
70 The overall detection efficiency (ODE) of this instrument, defined as the number of single particle mass spectra obtained from
71 the total number of aerosol particles in the sampled air, was determined to range from ~0.15% to ~2.2% for polystyrene latex
72 (PSL) particles with geometric diameters (d_p) between 350 nm and 800 nm (Gemayel et al., 2016; Marsden et al., 2016). The
73 instrument used by Gemayel et al. (2016) exhibited a maximum ODE of ~2.2% for PSL particle diameters of 450 nm, while ~1%
74 at 600 nm was the peak ODE reported by Marsden et al. (2016), but only after modification of the instrument. The response of



75 the LAAPTOF to spherical PSL particles smaller than 350 nm and bigger than 800 nm, and the response to other particle types
76 with different shapes, have not been investigated systematically. The scattering efficiency (SE), defined as the number
77 percentage of particles detected by light scattering compared to the number of particles in the sampled air in front of the
78 aerodynamic inlet lens (ADL) of the instrument (cf. Fig. 1), is determined by the laser diodes, the detection optics, as well as the
79 photomultiplier tubes (PMT), and has a strong influence on the ODE of the instrument. Therefore, several groups tried to
80 improve this part of the instrument. Marsden et al. (2016) modified the detection stage geometry by replacing the detection laser
81 with a fiber coupled 532 nm, 1 W Nd:YAG solid state laser system with a collimated laser beam, accomplishing an order of
82 magnitude improvement in light detection sensitivity to PSL particles with 500–800 nm diameter. Zawadowicz et al. (2017)
83 modified the optical path of the laser diodes with a better laser beam of <1 mrad full angle divergence and 1000 μm detection
84 beam spot size, and applied light guides to enhance the scattered light collection, resulting in 2–3 orders of magnitude
85 improvement in optical counting efficiency to PSL particles with 500–2000 nm vacuum aerodynamic diameter (d_{va}). There are
86 only very few studies so far that discuss mass spectral patterns of different particle types measured by LAAPTOF. Gemayel et al.
87 (2016) presented spectra from ambient particles collected in the city centre of Marseille, France; pure soot and SOA coated soot
88 particles (positive spectra only; Ahern et al., 2016). Spectra from potassium rich feldspar, soot, Argentinian soil dust, and
89 Snomax (commercial ice nuclei) were shown by (Zawadowicz et al., 2017), and PSL and potassium rich feldspar spectra were
90 measured by Marsden et al. (2017). Reitz et al. (2016) presented peak assignments for pure ammonium nitrate and sulphate
91 particles, as well as for ambient particles measured at a suburban site of Düsseldorf, Germany, but did not show any spectra.
92 Marker ions generated from SPMS are likely instrument specific, as pointed out by Schmidt et al. (2017). Therefore, there is a
93 need for publicly available spectral information of this relatively new instrument.

94 There exists several techniques to group the large number of individual particle types and spectra resulting from SMPS
95 measurements, such as k-means, c-means and hierarchical clustering algorithms, neural network based methods such as ART2-A,
96 as well as the most recent algorithm of ordering points to identify the clustering structure (OPTICS), to help analyse the data
97 (Hinze et al., 1999; Murphy et al., 2003; Reitz et al., 2016; Zelenyuk et al., 2006b; Zhao et al., 2008). For LAAPTOF data
98 analysis, the Fuzzy c-means algorithm is commonly used to do classification based on the similarities of the individual spectra.
99 The number of the classes is chosen manually (Hinze et al., 1999; Reitz et al., 2016). There also exist target (reference
100 spectra/predefined clusters)-oriented methods that are used for analysing single particle mass spectrometer data, especially for
101 ambient monitoring (Hinze et al., 1999; Gleanta GmbH; LAAPTOF AnalysisPro, Aeromegt GmbH).

102 In this paper we have characterized our LAAPTOF instrument with respect to its ODE for PSL, NH_4NO_3 , and sodium
103 chloride (NaCl) particles for a wide size range (d_m : 200–2000 nm PSL; 300–1000 nm NH_4NO_3 and NaCl). We present
104 laboratory based reference spectra for aerosol particles containing atmospherically relevant major components, which were
105 grouped in three categories: 1) particles consisting of pure compounds, e.g. NH_4NO_3 , K_2SO_4 , and organic acids; 2) particles
106 consisting of well-defined mixtures of pure salts and mixtures of organic compounds, e.g. α -pinene SOA, PSL internally mixed
107 with K_2SO_4 , and other core-shell type of particles; and 3) particles consisting of complex mixtures, e.g. soot and dust particles.
108 These reference spectra may provide also other users comprehensive references for comparison purposes, and thus better
109 interpretation of ambient data. A one-day example of field data interpretation based on these reference mass spectra will be given
110 in chapter 3.3 and compared to a Fuzzy clustering approach.



111 2 Methods

112 2.1 LAAPTOF

113 The LAAPTOF has been described in several recent publications (Ahern et al., 2016; Gemayel et al., 2016; Marsden et al., 2016,
114 2017; Reitz et al., 2016; Zawadowicz et al., 2017). Therefore, we only briefly review the general operation steps that yield size
115 and composition information of individual aerosol particles. The LAAPTOF instrument used in this study was delivered in April
116 2015 and may differ in a few technical aspects from earlier or later versions. A schematic of the main LAAPTOF components is
117 given in Fig. 1 Particles with a vacuum aerodynamic diameter (d_{va}) between ~ 70 nm and $2.5 \mu\text{m}$ are sampled with a sampling
118 flowrate of ~ 80 standard cubic centimetre per minute (SCCM), focused and accelerated by an aerodynamic lens, ADL (LPL-2.5,
119 Aeromegt GmbH) with close to 100% transmission efficiency for particles with d_{va} 100 nm to $2 \mu\text{m}$, then pass through the
120 particle time-of-flight (PTOF) chamber in which the individual particle can be detected by two sizing laser beams (405 nm
121 continuous wave, 40 mW) separated by 11.3 cm. Based on the particle time of flight between the two laser beams, its d_{va} can be
122 determined and recorded. After detection by the second sizing laser, a nanosecond (ns) excimer laser pulse (wave length: 193 nm,
123 pulse duration: 4 to 8 ns, maximum pulse energy: ~ 8 mJ, beam diameter: $\sim 300 \mu\text{m}$ when it hits the particle, power density: $\sim 10^9$
124 $\text{W}\cdot\text{cm}^{-2}$, ATLEX-S, ATL Lasertechnik GmbH) can be triggered to desorb and ionize particle compounds. A laser pulse energy of
125 4 mJ was used for all the measurements in this study. More details about the ionization region geometry are given by Ramisetty
126 et al. (2017). The resulting ions are analysed by a bipolar time-of-flight mass spectrometer (BTOF-MS; TOFWERK AG; mass
127 resolution of $m/\Delta m \sim 600$ to 800 at 184 Th, mass range $m/q=1$ up to ~ 2000 Th). The resulting cations and anions are detected by
128 corresponding microchannel plate arrays (MCPs), producing a pair of positive and negative spectra for each single particle.

129 For each type of laboratory generated aerosol particle, we measured at least 300 mass spectra. Data analysis is done via the
130 LAAPTOF Data Analysis Igor software (Version 1.0.2, Aeromegt GmbH). There are five main steps for the basic analysis
131 procedure: a) removal of the excimer laser ringing signal from the raw mass spectra; b) determination of the signal baseline; c)
132 filtering for empty spectra; d) mass calibration; and e) stick integration. Spectra-to-spectra differences in peak positions due to
133 variance in the position of particle-laser interaction complicate the mass calibrations. Details can be found in the supplementary
134 information (SI). Spectra presented in this paper were typically normalized to the sum of ion signal before further aggregation.

135 For the grouping of ambient data, we used two different classification methods. The Fuzzy c-means clustering algorithm is
136 embedded in the LAAPTOF Data Analysis Igor software and starts from random class centres. Particle spectra with a minimum
137 distance between their data vectors and a cluster centre will be grouped into this specific class (Hinz et al., 1999). Since each
138 spectrum can belong to multiple classes (Reitz et al., 2016) the resulting fraction/percentage for each class represents the
139 information about the degree of similarity between aerosol particles in one particular class, and not a number percentage. The
140 second method developed in this study is based on the correlation between each ambient spectrum and our reference spectra. The
141 resulting Pearson's correlation coefficient (r) is used as the criteria to group particles into different types (here we use "types"
142 instead of "classes" in order to differentiate these two classification methods). When r is above the threshold value 0.6, the
143 ambient spectrum is considered to have high correlation with the corresponding reference spectra. For simplification we chose 10
144 positive and 7 negative reference spectra. For example, we only use German soil dust as the reference for arable soil dust rather
145 than using four arable soil dust samples from different places. More details about the procedure for this method as well as the
146 corresponding equations and uncertainties estimation can be found in the supplementary information.

147 2.2 Aerosol particle generation



148 The aerosol particles measured in this study (Table S1) were generated in three different ways (cf. Fig.1). Samples for pure
149 particles (except SiO₂) and homogeneous and heterogeneous mixtures (except SOA) were dissolved in purified water and
150 nebulized (ATM 221; Topas GmbH) with dry synthetic air, passed through two diffusion dryers (cylinder filled with Silica gel,
151 Topas GmbH), and then size selected by a Differential Mobility Analyser (DMA 3080, TSI GmbH) before being sampled by
152 LAAPTOF (setup A). A condensation particles counter (CPC 3010, TSI GmbH) was used to record the particle number
153 concentration. SOA particles from ozonolysis (~6 ppm ozone) of α -pinene (~2.2 ppm), a common laboratory-based surrogate for
154 biogenic SOA (Saathoff et al., 2009), were formed in the 3.7 m³ stainless steel Aerosol Preparation and Characterization (APC)
155 chamber and then transferred into the 84.5 m³ simulation chamber AIDA (Aerosol Interactions and Dynamics in the Atmosphere)
156 of KIT (Saathoff et al., 2003). Soil dust samples were dispersed by a rotating brush generator (RGB1000, PALAS) and injected
157 via cyclones into the AIDA chamber. Sea salt particles were generated in different ways (Wagner et al., 2017) and sampled from
158 the AIDA chamber (setup B in Fig. 1). Soot particles from incomplete combustion of propane were generated with a propane
159 burner (RSG miniCAST; Jing Ltd.) and injected into and sampled from a stainless steel cylinder of 0.2 m³ volume. Ambient
160 aerosol particles from a rural site near Leopoldshafen, Germany (refer to section 2.3) were sampled through a PM_{2.5} inlet (SH 2.5
161 - 16, Comde-Derenda GmbH) with 1 m³ h⁻¹, a fraction of which was guided into the LAAPTOF (set up C in Fig. 1). Silica,
162 Hematite, Illite_NX, mineral dust, black carbon from Chestnut wood (University of Zürich, Switzerland), and urban dust and
163 diesel soot reference particles from NIST, were directly sampled from the headspace of their reservoirs.

164 2.3 Field measurement

165 Unusually high particle number concentrations, similar to downtown Karlsruhe (a city in southwest Germany), were observed
166 frequently northeast of Karlsruhe by particle counters on-board a tram wagon (www.aero-tram.kit.edu) intersecting the city
167 (Hagemann et al., 2014). To study the nature and to identify possible sources of these particles, their number, size, chemical
168 composition, associated trace gases and meteorological conditions were measured from July 15th to September 1st, 2016 at a rural
169 location (49°6'10.54"N, 8°24'26.07"E), next to the tram line north of the village of Leopoldshafen, Germany. LAAPTOF
170 measurements provided information on size and mass spectral patterns for individual particles. In this paper we use data from
171 one day as an example for the potential interpretation of LAAPTOF spectral data using reference spectra.

172 3 Results and Discussion

173 3.1 Determination of LAAPTOF performance parameters

174 3.1.1 Scattering efficiency, hit rate and overall detection efficiency for standard samples

175 In the literature there are two definitions of detection efficiency (DE) of SPMS used: one is equal to the scattering efficiency (SE)
176 of the detection lasers (Brands et al., 2011; Gaie-Levrel et al., 2012; Su et al., 2004; Zelenyuk and Imre, 2005; Zelenyuk et al.,
177 2009), while the other one is the product of SE and hit rate (HR) of the ablation/ionization laser (Su et al., 2004; Gemayel et al.,
178 2016; Marsden et al., 2016). The hit rate (HR) is the fraction of particles detected by the scattering optics leading actually to a
179 useful mass spectrum. In this paper we use overall detection efficiency (ODE), defined by the following equations:

$$\text{ODE} = \text{SE} \times \text{HR} \times 100\% \quad (1)$$

$$\text{SE} = N_d/N_0 \times 100\% \quad (\text{transmission efficiency of ADL is included}) \quad (2)$$



$$\text{HR} = N_s / N_d \times 100\% \text{ (ionization efficiency is included)} \quad (3)$$

$$N_0 = C_n \times \text{flowrate} \times \text{time} \quad (4)$$

180 where N_d is the number of particles detected by light scattering, N_0 is the number of particles in front of the ADL, N_s the number
181 of bipolar spectra, and C_n is the particle number concentration (cm^{-3}) measured by a CPC in front of the ADL. The sample
182 flowrate of the LAAPTOF is $\sim 80 \text{ cm}^3 \text{ min}^{-1}$.

183 HR, SE, and ODE for spherical PSL particles as a function of electrical mobility equivalent diameter d_m , are plotted in Fig. 2.
184 It should be noted that the LAAPTOF detection behaviour may vary depending on the alignment of the ADL and the optical
185 components (especially the detection laser diodes), which is difficult to reproduce. We therefore show results for PSL particles
186 based on 2 repeated experiments after 3 alignments each, and thus a total of 6 experiments for each data point. The uncertainty
187 intervals in Fig. 2 are the difference between the maximum/minimum and the average values obtained from these 6 experiments.
188 As shown in panel A of Fig. 2, for particle diameters from 200 to 400 nm, HR_{PSL} exhibits an increase from 69% to 94%,
189 decreases to 83% for 700 nm particles, and then becomes stable at $\sim 85\%$ for particles with diameters up to 2 μm . The average
190 HR_{PSL} ($\overline{\text{HR}}_{\text{PSL}}$) is $\sim 84\%$. SE_{PSL} and ODE_{PSL} show an M-like shape with two peaks, at 500 nm (SE_{PSL} 3.0%, ODE_{PSL} 2.7%), and at
191 1000 nm (SE_{PSL} 4.8%, ODE_{PSL} 4.2) (see panel B and C of Fig. 2). We attribute this behaviour to a combined effect of the
192 spherical shape of PSL particles and the optical system of this instrument, e.g. Mie resonances related to particle size and laser
193 wavelength (see section 3.1.2 for details). As shown in panel C of Fig. 2, values and trends of ODE_{PSL} in the size range of
194 300–800 nm of our instrument are similar to those reported by (Gemayel et al., 2016) and (Marsden et al., 2016) for their
195 LAAPTOF instruments. A recent LAAPTOF study by Zawadowicz et al. (2017) shows comparable results for PSL particles with
196 $d_p \leq 500 \text{ nm}$, and an M-like shape of ODE in the size range of 200–2000 nm (after instrument modification).

197 We also measured mass spectra of non-spherical NH_4NO_3 ($\chi=0.8$, Williams et al., 2013) and NaCl particles (cubic, $\chi=1.06$ to
198 1.17, Zelenyuk et al., 2006a). Similar as for PSL particles, NH_4NO_3 , and NaCl particles show relatively high and stable HR with
199 average values of 80% and 66% (see panel D in Fig. 2), thus SE and ODE have a similar trend. No M-like shape of ODE as a
200 function of particle size is observed due to the different light scattering properties of the non-spherical salt particles (Bohren and
201 Huffman, 2007) (see panels E and F in Fig. 2). Comparable results were shown for $(\text{NH}_4)_2\text{SO}_4$ particles ($\chi=1.03$ to 1.07,
202 Zelenyuk et al., 2006a) by Zawadowicz et al. (2017). As shown in Fig. 2 E–F, SE and ODE decrease with increasing shape factor
203 for salt particles of the same size. We will discuss this in more detail in the following section.

204 3.1.2 Factors influencing overall detection efficiency

205 There are various factors that can influence the ODE. One of these is particle size. For particles with diameters below 200 nm,
206 the scattered light becomes too weak to be detected due to the strong dependence of the scattering intensity on particle size
207 (Bohren and Huffman, 2007). For particles with diameters larger than 2 μm , focusing by the ADL is much less efficient,
208 resulting in a higher divergence of the particle beam. This lowers the probability of larger particles to be detected by the
209 detection/scattering laser and/or to be hit by the ionization laser. In addition, light scattering of spherical particles like PSL
210 changes from Rayleigh to Mie to Geometric scattering as the size parameter $\alpha = \pi d_p / \lambda$ increases from $\ll 1$ to ~ 1 to $\gg 1$ (Seinfeld
211 and Pandis, 2006). α ranges from ~ 1.5 to 19 for 200–2500 nm PSL particles, and is thus in the Mie scattering regime and the
212 reason for the M-like shape of SE_{PSL} and ODE_{PSL} . As long as the particle diameter (d_p) is smaller than the wavelength of the
213 detection laser light, here 405 nm, the scattered radiation intensity (proportional to d_p^6) will rapidly decrease with decreasing
214 particle sizes, resulting in low ODE. ODE is e.g. 0.01% for 200 nm PSL particles. For non-spherical particles like salts, their SE



215 and ODE are also size dependent (panel F in Fig. 2), due to size-dependent light scattering ability and particle beam divergence.
216 However, they don't exhibit Mie resonance, and thus don't show an M-like shape in their scattering efficiency.

217 Optical properties of the particles have a strong impact on how light is scattered and absorbed, and thus also greatly influence
218 scattering efficiency and ionization efficiency (or hit rate), respectively. As shown in Fig. 2, ODE for NH_4NO_3 is higher than that
219 for NaCl at any size we studied (panel F). This is caused by differences in their optical properties and shapes. The reference
220 spectra of pure NH_4NO_3 and $(\text{NH}_4)_2\text{SO}_4$ particles showed intensive prominent peaks for pure NH_4NO_3 particles but only one
221 weak peak for pure $(\text{NH}_4)_2\text{SO}_4$ particles. This is indicating that NH_4NO_3 is a better absorber than $(\text{NH}_4)_2\text{SO}_4$, and thus easier to
222 ablate and ionize. For homogeneous mixtures of these two ammonium salts, the sulphate species are detected much more easily
223 due to increased light absorption by the nitrate component (refer to section 3.2.2). Soot particles are good light absorbers and
224 thus relatively easy to ablate and ionize. However they scatter only little light due to the small size (typically ~ 20 nm) of the
225 primary particles forming their agglomerates, and are thus hardly detected. Their usually small size is an additional disadvantage
226 for their detection. Some small organic compounds with weak absorption properties are hard to ablate and ionize as well, e.g.
227 oxalic acid ($\text{C}_2\text{H}_2\text{O}_4$), pinic and cis-pinonic acids measured in this study had much weaker signals in the spectra ($\sim 80\%$ lower)
228 than macromolecular organic compounds in PSL or humic acid particles.

229 Particle morphology is another important factor. The scattering efficiency for non-spherical NH_4NO_3 is higher than for
230 spherical PSL particles in the size range of 300–800 nm (Fig. 2 B–E) (Ackerman et al., 2015). For larger particle sizes ($d_m > 800$
231 nm), beam divergence offsets the shape effect (Murphy, 2007). Apart from that, the increase of surface roughness and
232 inhomogeneity can promote the scattering capability of particles (Ackerman et al., 2015).

233 The incident intensity of radiation, which is another parameter that influences the light scattered by particles (as well as
234 background signal caused by stray light), is related to power and beam dimensions of the laser. A laser power of 40 mW was
235 used in this study. Marsden et al. (2016) replaced the detection laser with a fibre coupled 532 nm, 1 W Nd:YAG solid state laser
236 system that has a collimated laser beam, resulting in an order of magnitude improved sensitivity to PSL particles with 500–800
237 nm diameter. Zawadowicz et al. (2017) used laser diodes with a laser beam of <1 mrad full angle divergence and 1000 μm
238 detection beam spot size, and applied light guides to enhance the scattered light collection, resulting in 2–3 orders of magnitude
239 improvement in optical counting efficiency of PSL particles with d_{va} 500–2000 nm. In addition, alignment of the excimer laser
240 focus in x, y, and z position influences optimum hit rates (Ramisetty et al., 2017).

241 There are further instrumental aspects that affect the detection efficiency. High number concentrations of the incoming
242 particles influence the ODE, since there can be more than one particle present between the two detection lasers. The transmission
243 efficiency of the ADL is included in the scattering efficiency, and thus directly influences it. The size range of particles focused
244 in the lens, and the particle beam width strongly depend on the configuration of the ADL (Canagaratna et al., 2007; Johnston,
245 2000). Liu lenses and Schreiner lenses can focus the particles in the size range of 80–800 nm, and 300–3000 nm, respectively
246 (Kamphus et al., 2008; Liu et al., 1995; Schreiner et al., 1999). The ADL transmission efficiency of our instrument, as
247 determined by the manufacturer (Aeromegt GmbH), is close to 100% for particles with d_{va} 100–2000 nm.

248 3.2 LAAPTOF reference spectra of laboratory generated particle types

249 Particles for which reference spectra are presented here are listed in Table S1. For each type of these aerosol particles, we present
250 averaged spectra for typically 300 to 500 single particles. The relative standard deviations (RSD, SD normalized to signal) for
251 the characteristic peaks are in the range of 15–186%, median value 77%.



252 Despite the lack of full quantitiveness of the LAAPTOF, mass spectral signal amplitudes show an increase with particle
253 size. However, no systematic changes in the mass spectral signatures were observed for different particle sizes. Therefore,
254 particles in the optimum size range of the LAAPTOF ($d_m = 800$ nm) and with good signal-to-noise ratio were chosen to generate
255 reference spectra. For polydisperse particles generated in the AIDA chamber, the corresponding average spectra include particles
256 of broader size distributions compared to those preselected by the DMA. Information on particle generation or source as well as
257 the sizes is listed in Table S1.

258 A qualitative comparison between the relative peak intensity ratios within an single particle spectrum and those in another
259 spectrum can yield relative quantitation information, as suggested by Gross et al. (2000). We add information on typical peak
260 ratios to some of our reference spectra to help identify specific species.

261 3.2.1 Pure compound particles

262 Although particles consisting of one single species only are rarely sampled in the atmosphere, interpretation of mass spectra of
263 ambient samples is supported by the knowledge about the mass spectra of pure compounds. In the following mass spectra for a
264 few typical ambient aerosol constituents are discussed.

265 Figure 3 shows average spectra for pure compound aerosol particles. For NH_4NO_3 particles (panel A), we observed the
266 positive ions m/z 18 NH_4^+ and m/z 30 NO^+ ; and the negative ions m/z 46 NO_2^- and m/z 62 NO_3^- , similar to Reitz et al. (2016).
267 The LAAPTOF is much less sensitive to ammonium than nitrate fragments, leading to a weak NH_4^+ signal and prominent NO^+ ,
268 NO_2^- and NO_3^- peaks. The ratio of NO^+ to NH_4^+ is ~ 48 , and the ratio of NO_2^- to NO_3^- is ~ 4 . The prominent peak of NO^+ arises not
269 only from nitrate (majority), but also from ammonium (Murphy et al., 2006). In our ammonium nitrate spectra, there are weaker
270 signatures of m/z 46 NO_2^+ and m/z 125 $\text{HNO}_3\text{NO}_3^-$ (not shown here, but visible and reproducible), which were also observed in
271 PALMS mass spectra (Zawadowicz et al., 2015). For K_2SO_4 particles, we observed the potassium signals at m/z 39 K^+ and m/z
272 41 K^+ , and a sulphate signature with ion clusters grouped around m/z 32 S^- , m/z 64 SO_2^- , m/z 80 SO_3^- and m/z 96 SO_4^- . Note that
273 peaks with high intensity exhibit “ringing” in the raw spectra, resulting in small peaks beside the main ones in the integrated
274 stick spectra, such as m/z 40⁺ besides m/z 39 K^+ in Fig. 3 (B), and m/z 36⁻ besides m/z 35 Cl^- in the spectra for sodium chloride
275 NaCl (Fig. S1). Therefore, the real intensities of m/z 39 K^+ and m/z 35 Cl^- should include their corresponding side ringing peaks.
276 The ratio of m/z 39 K^+ to m/z 41 K^+ is ~ 13.2 , close to the natural isotopic ratio of ~ 13.9 for $^{39}\text{K}/^{41}\text{K}$. For pure NaCl particles, the
277 ratio of m/z 35 Cl^- to m/z 37 Cl^- is ~ 3.2 , similar to the natural isotopic ratio of ~ 3.1 for $^{35}\text{Cl}/^{37}\text{Cl}$. Therefore, these two isotopic
278 ratios can be used as markers to identify K and Cl measured by LAAPTOF. Another inorganic compound measured here is silica
279 (Fig. S2) with the typical peak ratio (~ 1.0) of m/z 76 $\text{SiO}_3^- + m/z$ 77 HSiO_3^- to m/z 60 SiO_2^- . The corresponding histograms of
280 such ratios for different particle samples can be found in Fig. S3.

281 High signal intensities in oxalic acid spectra are observed at m/z 18 H_2O^+ , 28 CO^+ , and 30 CH_2O^+ , as well as some weaker
282 peaks at m/z 40⁺, 44⁺, 56⁺, and 57⁺. M/z 89 $\text{C}_2\text{O}_4\text{H}^+$ is used as signature ion for oxalic acid in other SPMS studies (Roth et al.,
283 2016). In our study, a distinct signal at around m/z 89⁻ is observed as well, indicating oxalate fragment formation after laser
284 ablation.

285 In order to identify humic like substances in the ambient particles, we measured humic acid particles (Fig. S4) and found
286 hydrocarbon and elemental carbon fragments, with very prominent peaks at m/z 24⁻, 25⁻, and 26⁻ suggested to be organic ions
287 (Silva et al., 2000), as well as peaks at m/z 25⁻, 26⁻, 49⁻, and 73⁻ for unsaturated organic compounds.

288 3.2.2 Particles consisting of well-defined internal mixtures



289 Figure 4 shows average spectra from homogeneously internally mixed particles. The spectrum from the mixture of NH_4NO_3 and
290 $(\text{NH}_4)_2\text{SO}_4$ (panel A) contains the signature from pure NH_4NO_3 particles, but with lower relative intensities (each peak intensity
291 is normalized to the sum of ion signal) for NO_2^- and NO_3^- , due to the formation of anion clusters at $\sim m/z=80 \text{ SO}_3^-$ and 97 HSO_4^- .
292 In addition, compared to the pure NH_4NO_3 particles, the ratio of NO^+ to NH_4^+ (~ 34) is $\sim 30\%$ lower in the spectrum for the
293 mixture, due to its lower molar ratio of nitrate/ammonium, whereas the ratio of NO_2^- to NO_3^- (~ 7) is 80% higher. Nitrate is
294 believed to assist in light absorbing for the mixed particles, resulting in a sulphate signature that could not be observed for pure
295 $(\text{NH}_4)_2\text{SO}_4$. This exemplifies potential effects of individual particle chemical composition on mass spectral performance of the
296 LAAPTOF. For the mixture of K_2SO_4 and NaCl (panel B), similar signatures as for the pure particles were observed. Compared
297 to the pure NaCl particle spectra, the signal intensity of Na^+ is decreased. This can be explained by more cations formed from the
298 mixed particles, including from potassium, which has a higher ionization potential and lower lattice energy than NaCl . For the
299 mixed particles, expected clusters such as $113/115 \text{ K}_2\text{Cl}^+$, 109 KCl_2^- , and 119 NaSO_4^- and a minor fragment 97 KNaCl^+ were
300 observed, but not $81/83 \text{ Na}_2\text{Cl}^+$ as found in pure NaCl particles. These results show that compared to pure compounds, mass
301 spectra from aerosol particles consisting of mixtures can feature new ions, while some marker ions for the pure compounds may
302 disappear. These spectra are thus not simply a combination of the spectra from single component particles. Another example for
303 an inorganic mixture of NH_4NO_3 and K_2SO_4 is provided in Fig. S5. The α -pinene SOA spectrum is shown in panel (C) of Fig. 4.
304 Ablation of α -pinene SOA particles forms different types of organic fragments: 1) hydrocarbon and oxygenated organic
305 fragments $\text{C}_x\text{H}_y\text{O}_z$, ($x=1-6$, $y=0-9$, $z=0-3$, details about the peak assignments can be found in Table S2), except for m/z 59^+ , 83^+ ,
306 85^+ , and 95^+ , are comparable to the combination mass spectral patterns for *cis*-pinonic and pinic acids (refer to Fig. S6) which are
307 oxidation products from α -pinene ozonolysis (Saathoff et al., 2009; Yu et al., 1999); 2) Carbon clusters 12 C^+ , 24 C_2^+ , 36 C_3^+ ,
308 and 60 C_5^+ , with the most prominent peak in 12C^+ , assigned to both soot and organic matter fragments in another LAAPTOF
309 study (Ahern et al., 2016); 3) Carboxylic acid groups in the negative spectra, e.g. 45 COOH^- , $59 \text{ CH}_2\text{COOH}^-$, $73 \text{ C}_2\text{H}_4\text{COOH}^-$, 85
310 $\text{C}_3\text{H}_4\text{COOH}^-$ and $99 \text{ C}_4\text{H}_6\text{COOH}^-$.

311 Figure 5 (A) shows the spectrum for heterogeneously internally mixed K_2SO_4 and PSL particles (PSL core, K_2SO_4 shell). All
312 signatures for PSL particles, i.e. hydrocarbon fragments in positive spectra, intensive organic signature m/z 24^+ , 25^+ , and 26^+ ,
313 carbon clusters $\text{C}_n^{+/-}$, and m/z 49^- and 73^- fragments arising from unsaturated structures such as aromatic structures are retained in
314 this spectra (grey labels), and the corresponding peak intensities are similar to the pure PSL particles (refer to Fig. S7). However,
315 the intensities of most of the K_2SO_4 fragments weaker compared to pure K_2SO_4 particles, likely due to the quite thin or only
316 partial coating layer of K_2SO_4 on the PSL core (the nominal geometric size of the PSL particles mixed with the aqueous solution
317 of K_2SO_4 was 800 nm which is the same size that was selected by the DMA prior to sampling by the mass spectrometer.). The
318 most prominent peak at m/z 39^+ with a normalized intensity of ~ 0.46 , containing both K^+ and C_3H_3^+ fragments, is mainly
319 attributed to K^+ (intensity ~ 0.73 for pure K_2SO_4), since the intensity of C_3H_3^+ (~ 0.06) for pure PSL is much lower (refer to Fig.
320 S9). The still intensive signal from 39 K^+ despite the weaker sulphate peaks corresponds to the high sensitivity of the instrument
321 for potassium. Fig. 5 (B) shows the average spectrum for poly(allylamine hydrochloride) coated gold particles. Prominent
322 signatures of nitrogen containing compounds (NOCs) is observed at m/z $58 \text{ C}_2\text{H}_5\text{-NH-CH}_2^+$, 15 NH^+ , 26 CN^- , and 42 CNO^- , as
323 well as the signatures for unsaturated organic compounds at m/z 25^- , 26^- , 49^- , and 73^- . Strong intensities for m/z (35^- plus 36^-)
324 and 37^- with ratio of ~ 3.1 can be assigned to Cl isotopes derived from the hydrochloride. We also observed small gold peaks at
325 m/z $197^{+/-}$ both in positive and negative spectra.

326 Mass spectra for other well-defined compounds, i.e. synthetic hematite and pure sea salt particles, are also provided in the
327 supplementary information (Fig. S8 and S9).



328 3.2.3 Particles consisting of complex mixtures

329 Figure 6 shows the average spectra for different types of soot particles. All of them show characteristic patterns for elemental
330 carbon (EC) $C_n^{+/}$. For soot1 with high organic carbon (OC) content from propane combustion in the laboratory (panel B),
331 prominent peaks were observed at m/z 28 CO^+ and 27 $C_2H_3^+$, as well as some other organic carbon signatures at m/z 39⁺, 40⁺, 44⁺
332 and 56⁺. All the organic signatures in soot1 with high OC were also observed for soot3, lignocellulosic char from Chestnut wood
333 (panel D), indicating that biomass burning soot contains a significant fraction of OC. It should be noted that biomass burning will
334 also form potassium, thus m/z 39⁺ contains both K^+ and $C_3H_3^+$ fragments. M/z 24⁻, 25⁻ and 26⁻ can be observed in all the soot
335 types, but with a bit different patterns: 1) soot with high EC content shows very high m/z 24⁻ (~2 to 3 times than m/z 25⁻), while
336 2) soot with high OC shows comparable or even higher m/z 25⁻ to than m/z 24⁻. These patterns might provide help to distinguish
337 EC and OC contributions in the spectra from ambient particles.

338 Figure 7 shows spectra for Arizona test dust (milled desert dust) (panel A), arable soil SDGe01 sampled from Gottesgabe in
339 Germany (B), and agricultural soil dust collected from harvesting machines after rye and wheat harvest (C). For Arizona test dust,
340 we observed high mineral signatures of aluminium and silicon containing clusters, namely 27 Al^+ , 28 Si^+ , 44 SiO^+ , 43 AlO^+ , 59
341 AlO_2^+ , 60 SiO_2^+ , 76 SiO_3^+ , 119 $AlSiO_4^+$, 179 $AlSiO_4.SiO_2^+$, 136 $(SiO_2)_2O^+$. It should be noted that high 16 O^- and 17 OH^-
342 accompany the intensive mineral signatures, attributed to the adsorbed water on the active surface of mineral particles. In
343 addition, other mineral related metal clusters, e.g. 7 Li^+ , 23 Na^+ , 24 Mg^+ , 40 Ca^+ , 39/41 K^+ , 55 Mn^+ , 56 Fe^+ , 58 Ni^+ , 64 Cu^+ ,
344 metal oxides and hydroxides, 56 CaO^+ , 57 $CaOH^+$, 96 Ca_2O^+ , 112 $(CaO)_2^+$, and 88 FeO_2^+ , as well as weak anion clusters of
345 organic signature (m/z 24 C_2^- , 25 C_2H^- , 26 $C_2H_2^-$, and 42 $C_2H_2O^-$), NOCs (m/z 26 CN^- and 42 CNO^-), chloride (m/z 35⁻ and 37⁻),
346 sulphate (m/z 32⁻, 48⁻, 64⁻, 80⁻, and 97⁻), phosphate (63 PO_2^- and 79 PO_3^-), diacids (oxalate 89 $(CO)_2OOH^-$ and 117 $(CO)_3OOH^-$)
347 and an unknown fragment m/z 148⁻ were observed in the spectra (A). M/z 26⁺ in panels (B) and (C) is much higher than m/z 24⁻
348 and 25⁻, due to the contribution of CN fragments from NOCs. Similar signatures can also be observed in the spectra for Saharan
349 desert dust (Fig. S10).

350 For soil dust, most of their mineral and organic fragments are similar as desert dust, however with different intensities, e.g.
351 m/z 24⁻, 25⁻, 26⁻, and 42⁻ (labelled in green) are more intensive than those in desert dust, indicating higher organic compound
352 content. Some peak ratios of fragments are similar across the different dust types, e.g. 40 Ca^+ to 56 CaO^+ is 2.2, 1.1, and 2 for
353 desert dust, arable soil dust and agricultural soil dust, respectively. Compared with desert dust, there are different fragments from
354 soil dust particles, e.g. EC patterns (labelled in grey), organic acids signatures (blue), ammonium signatures (orange),
355 unsaturated organic fragments (m/z 49⁻ and 73⁻) and some other unknown fragments (red). For arable soil dust particles, we also
356 measured samples from Paulinenaue in Germany (SDPA01), Argentina (SDAr08) and Wyoming in USA (SDWY01) (refer to
357 Fig. S11). Dominant mass spectral peak patterns are similar across all soil dust samples. They are located at around m/z 27⁺, 39⁺,
358 and 56⁺ in the positive spectra; and 26⁻, 42⁻, 60⁻, and 76⁻ in negative spectra. Less prominent but reproducibly detected are
359 carboxylic acid groups (e.g. $COOH^-$) and EC patterns. German soil dust, however, contains more organic species than the soil
360 dusts from Argentina and the USA according to the intensities of m/z 24⁻, 25⁻, and 26⁻, while Argentinean soil dust contains
361 much less mineral species comparing the mineral signatures e.g. 27⁺, 28⁺, 40⁺, 44⁺, and 56⁺. The ratios of m/z 39 K^+ and 41 K^+
362 (3.6, 3.8, 3.5, 5.3 for SDGe01, SDPA01, SDAr08, and SDWY01, respectively) are much lower than the typical peak ratio (~10.6)
363 for potassium (Table 1), indicating that they are likely contributed to by both potassium isotopes and hydrocarbon fragments.

364 For agricultural soil dust particles, obviously ammonium (m/z 18 NH_4^+ and 30 NO^+), phosphate (m/z 63 PO_2^- , 79 PO_3^- , and
365 95 PO_5^-) and potassium signatures (m/z 39 K^+ and 41 K^+) can be found in the spectra, attributed to fertilization. Apart from that,
366 typical biological signatures were observed: 1) the strong m/z 26⁻, 42⁻, and 39⁺ pattern is similar to the potassium organo-



367 nitrogen particle type observed by an ATOFMS at an urban site in Barcelona (Dall'Osto et al., 2016), and which were assigned to
368 carbohydrates, arising from biogenic species (Schmidt et al., 2017; Silva et al., 2000). 2) 26^- and 42^- could also be contributed by
369 CN^- and CNO^- derived from NOCs, i.e. amines, as well as m/z 30 CH_3NH^+ , 58 $C_2H_5NHCH_2^+$, and 59 $(CH_3)_3N^+$. These biological
370 signatures have also been observed by ALABAMA in the field (Schmidt et al., 2017). 3) Some weak but reproducibly detected
371 fragment pattern at around m/z 77 $C_6H_5^+$, 91 $C_7H_7^+$, 103 $C_8H_7^+$, 105 $C_8H_9^+$, and 115 $C_9H_7^+$ might be originate from aromatic
372 compounds. Similar patterns can also be found for PSL particles (Fig. S7).

373 Other examples for complex mixtures, i.e. illite and sea salt particles with biological components are provided in the
374 supplementary information (Fig. S12 and S9).

375 All the peak assignments and mass spectral patterns like signature peaks as well as some stable peak ratios mentioned above
376 have been summarized in Table S2 and Table 1, respectively. We consider these laboratory-based reference spectra as useful for
377 the analysis of data obtained also by other LAAPTOF versions and to some extent even for other single particle mass
378 spectrometers. Similar mass spectra are to be expected as long as they use similar ablation & ionization laser pulses (4 mJ, 193
379 nm), inlet regions for the mass spectrometer, and mass spectrometer types. In the near future, we plan to make these laboratory-
380 based reference spectra publicly available via the EUROCHAMP-2020 data base (www.eurochamp.org).

381 3.3 Interpretation of field data

382 Figure 8 shows an example of bipolar mass spectra for six different particle classes measured in the field campaign at a rural site
383 near Leopoldshafen in southwest Germany. On July 29th, 2016 within 24 hours, 7314 particles were detected, successfully
384 ablated and mass spectra generated by LAAPTOF. The 7314 pairs of spectra were then clustered by the Fuzzy c-means
385 algorithm, resulting in six classes. The resulting number of classes with clearly different features depends on the experience of
386 the operating scientist to identify them (please refer to the details of Fuzzy clustering procedure in the supplementary
387 information). The Fuzzy results are compared with the laboratory-based reference spectra by calculating their correlation
388 coefficients (cf. Fig. 9). All classes exhibit a sulphate signature with m/z 97 HSO_4^- and m/z 80 SO_3^- ; a nitrate signature with m/z
389 46 NO_2^- and 62 NO_3^- ; an organic compound signature with m/z 24 C_2^- , 25 C_2H^- , and 26 C_2H_2/CN^- ; and a NOC signature with
390 m/z 26 CN^- and 42 CNO^- in the negative spectra. More characteristic signatures for each particle class can be observed in the
391 positive spectra. All particles measured on this day show a 35% similarity to class 5 with obvious signatures for potassium (K)
392 and sulphate, with significant correlation with the reference particles containing potassium and sulphate (Fig. 9). Besides, class 5
393 also has significant correlation with some other cations arising from ammonium, organic compounds, and dust. The ratio of m/z
394 ($39^+ + 40^+$) to 41^+ is ~ 11 , close to the value for pure K_2SO_4 particles (~ 13.5), thus we assigned them to K^+ rather than organic
395 fragments. Further, there is a 15% similarity to class 4 with prominent ammonium signatures at m/z 18 NH_4^+ and 30 NO^+ ,
396 sulphate signatures, as well as a relatively weaker but reproducible nitrate signature. The corresponding spectrum is similar as
397 the spectrum for the homogeneous mixtures of NH_4NO_3 and $(NH_4)_2SO_4$ (panel A in Fig. 4). This class also has strong correlation
398 with both positive and negative reference spectra for the mixture of ammonium nitrate and ammonium sulphate particles.
399 Ammonium, nitrate and sulphate are the major secondary inorganic species in atmospheric aerosol particles (Seinfeld and Pandis,
400 2006), thus we name this class "secondary inorganic". It should be noted that this class has significant correlation with
401 ammonium and cations arising from oxalic acid, however class 4 has weak correlation with the signature cation, i.e. m/z 89
402 $C_2O_4H^-$ (oxalate), of oxalic acid. Therefore, we can rule out a significant contribution of oxalic acid. There is also a 15%
403 similarity to class 2 (sodium rich), with a characteristic pattern of a strong signal at m/z 23 Na^+ accompanied by two weaker
404 peaks at m/z 39 K^+ (with typical potassium peak ratio of ~ 12) and 63^+ (might contain both Cu^+ and $C_5H_3^+$ fragments). Class 2 has



405 significant correlation with the cations (i.e. Na and K) arising from sea salt, but weak correlation with its anions, such as m/z 35⁻
406 and 37⁻ chloride isotopes. A sea salt contribution can thus be ruled out. Its negative spectrum significantly correlates with nitrate,
407 sulphate, and dust particles. Besides sodium rich dust aged sea salt may be an appropriate classification. Class 3 is named “aged
408 soot”, since it has significant correlation with soot particles, especially diesel soot, and a prominent sulphate signal. This class
409 has an EC pattern with m/z 12n C_n^+ , similar to those in the reference spectra for soot particles (Fig. 6) as well as the reference
410 spectra for PSL particles (Fig. S9). The patterns at m/z 27 $C_2H_3^+$ and 28 CO^+ , m/z 36 C_3^+ and 39 $C_3H_3^+$ as well as the m/z 24⁻, 25⁻
411 and 26⁻ with higher m/z 26⁻, indicate an OC contribution. This is supported by the correlations especially with PSL particles but
412 also several other organic compounds, suggesting that this class of particles contains organic species. Class 6 is dominated by
413 calcium (Ca) and sulphate with characteristic calcium signature peaks at m/z 40 Ca^+ and 56 CaO^+ , also found in the spectra for
414 dust particles (Fig. 7, Fig. S10, and S11). M/z 40⁺ and 56⁺ may also contain 40 C_2O^+ and 56 $Fe/C_4H_8^+$ fragments, respectively.
415 Class 1 contains almost all fragments observed in other classes, and is thus named “more aged /mixed particles”. As shown in
416 Fig. 9, class 6 is consequently correlated with almost all of the reference spectra (both positive and negative ones).

417 In order to further interpret the field data, we also classified the ambient mass spectra only based on correlation with 17
418 selected laboratory-based reference spectra (10 positive + 7 negative spectra) listed in Table S3. This approach resulted in 13
419 particle types, 7 more than were distinguished by Fuzzy clustering. It should be mentioned that at the beginning we were able to
420 identify all but the Ca rich particle class resulting from Fuzzy clustering, since initially we did not have a reference for this type.
421 We therefore used class 6 as an additional reference spectrum for this type of particles, which is among one of the 13 types.
422 Initially, using a Pearson’s correlation coefficient r of ≥ 0.6 as threshold for classification resulted in 21 main types of particles
423 (here we use “types” instead of “classes” in order to differentiate these two classification methods), with particle number
424 fractions $>1\%$. The corresponding histogram of these 21 particle types is shown Fig. S13. These 21 types were then manually
425 aggregated after observing their spectra and reduced to 13. Similar as the Fuzzy class number, the resulting number of
426 characteristic types also strongly depends on the expert experience to identify them (please refer to the details of reference
427 spectra-oriented grouping procedure in the supplementary information) Their corresponding spectra are shown in Fig. 10. All the
428 types above the dashed line (A to I) exhibit more prominent secondary inorganic signatures (m/z 97 HSO_4^-) and higher number
429 fractions than the ones below the dashed line. Although particle types A-I all exhibit a more prominent sulphate pattern with m/z
430 80 and 97 than nitrate pattern with m/z 46 and 62, they are higher correlated with the mixture of nitrate and sulphate than either
431 of them. Therefore, we assign the corresponding types to nitrate and sulphate. All the types in the lower panels (J to M) have
432 significant correlation with arable soil dust in the negative spectra, which have organic signatures, e.g. m/z 24⁻, 25⁻, and 26⁻, as
433 well as some mineral signatures like m/z 119⁻. Compared with the negative spectra, the positive spectra are more characteristic,
434 which was also observed in the Fuzzy results. Type A, B, C, D, and E are comparable with Fuzzy class 5, 4, 2, 6, and 3,
435 respectively (the correlation coefficients are 0.89 for type A and class 5, 0.95 for type B and class 4, 0.84 for type C and class 2,
436 0.76 for type D and class 6, and 0.81 for type E and class 3). Types F to I are more similar to aged/mixed particles, with more
437 fragments compared to types A to E. Type H is comparable with Fuzzy class 1. ~10% of the particles cannot be grouped into any
438 type due to spectrum-to-spectrum peak shifts. As shown in the spectra in both Fig. 9 and 10, all organic species were internally
439 mixed with inorganic species.

440 This reference spectra-based classification can also be used for identification of particles with low number fractions among
441 the huge amount of ambient data, and for selection of particles containing particular species e.g. for which the instrument has a
442 lower sensitivity. This can be achieved by e.g. excluding peaks with high signal such as m/z 39 $K/C_3H_3^+$, or selecting a certain
443 particle size range, or mass range. As an example, 55 lead containing particles (Pb, with isotopes at m/z 206, 207, and 208)



444 (details are given in the supplementary information) were identified among the 7314 ambient aerosol particles. The resulting
445 spectra of particle classes/types in one field study can also be used as reference for other studies. More applications of these
446 procedures for field data interpretation will be presented in an upcoming paper.

447 In short, Fuzzy and reference spectra-based classifications have some comparable results with high correlations (r : 0.76–0.95)
448 and also have different advantages: Fuzzy classification can identify special ambient particle types without any existing reference
449 if they have a significant abundance and signal strength, while reference spectra-based methods can identify target particle types
450 even with little abundance. They are complementary to some extent and thus their combination has the potential to improve
451 interpretation of field data.

452 4 Conclusions

453 In this study, the overall detection efficiency (ODE) of LAAPTOF was determined to range from $\sim(0.01 \pm 0.01)\%$ to $\sim(6.57 \pm$
454 $2.38)\%$ for polystyrene latex (PSL), ammonium nitrate (NH_4NO_3) and sodium chloride (NaCl) particles in the size range between
455 200 and 2000 nm. This is a relative good detection efficiency compared to earlier versions of the instruments especially when
456 considering the good reproducibility and stability even during field measurements. A comparison to other single particle mass
457 spectrometers is subject of another study and will be discussed in a separate publication. In any case matrix effects from aerosol
458 particles (e.g. size, morphology and optical property) and certain instrument influences (e.g. aerodynamic lens, detection system)
459 and their interaction must be taken into account to evaluate the LAAPTOF performance.

460 In order to facilitate the interpretation of single particle mass spectra from field measurements, we have measured various
461 well defined atmospherically relevant aerosol particles in the laboratory and provide here laboratory-based reference spectra for
462 aerosol particles of different complexity with comprehensive spectral information about the components (such as organic
463 compounds, elemental carbon, sulphate, nitrate, ammonium, chloride, mineral compounds, metals, etc. as commonly observed in
464 atmospheric aerosol particles). Our results show that the interpretation of spectra from unknown particle types is significantly
465 supported by using known mass spectral patterns like signature peaks for ammonium, nitrate, sulphate, and organic compounds
466 as well as typical peak ratios for e.g. potassium, silicon, and chlorides. Spectra for internally mixed particles may show new
467 clusters of ions, rather than simply a combination of the ions from single component particles. This may be a complication for
468 data interpretation which can be overcome if suitable reference spectra for correspondingly mixed particles are available.
469 Organic compounds generally have some ions in common but exhibit variations depending on the compound. Several peaks can
470 originate from different fragments, m/z 26⁻ and 42⁻ could be CN^- and CNO^- and/or C_2H_2^- and $\text{C}_2\text{H}_2\text{O}^-$, m/z 39⁺ and 41⁺ could e.g.
471 originate from K^+ isotopes or organic fragments, and organic matter can also be ionized to form the typical elemental carbon
472 pattern with $\text{C}_n^{+/-}$ ions. Hence the interpretation is not always unambiguously possible for such particles but may require
473 additional information (e.g. size, additional marker peaks, or even higher resolution spectra) or comparison to data from other
474 instruments like on-line aerosol mass spectrometers (e.g. AMS) or chemical ionization mass spectrometers (e.g. FIGAERO-
475 CIMS).

476 A set of mass spectra obtained in one day of field measurements was used for particle type classification based on Fuzzy
477 clustering and on the new reference spectra presented in this work. The corresponding 7314 spectra were clustered by a Fuzzy c-
478 means algorithm, resulting in six different similarity classes. The independent classification of the ambient mass spectra based on
479 17 selected reference spectra resulted in 13 different particle types which included those classes obtained by Fuzzy clustering.
480 Compared with the reference spectra, we found that each class has a sulphate signature at m/z 80 SO_3^- and 97 HSO_4^- , a nitrate



481 signature at m/z 46 NO_2^- and 62 NO_3^- , an organic compound signature at m/z 24 C_2^- , 25 C_2H^- and 26 $\text{C}_2\text{H}_2/\text{CN}^-$ and a nitrogen-
482 containing organic signature at m/z 26 CN^- and 42 CNO^- . Furthermore, we have performed target-oriented classification by using
483 a selected reference spectrum, which demonstrates the possibility to identify particles with low number fraction among the huge
484 amount of ambient data, e.g. lead-containing particles.

485 We conclude that the reference spectra presented in this paper are useful for interpretation of field measurements and for
486 understanding the impact of mixing on typical mass spectral signatures. Furthermore, the reference spectra should be useful for
487 interpretation of data obtained by other LAAPTOF versions or other single particle mass spectrometers using a similar ionization
488 method and comparable mass spectrometers. For future experiments using the LAAPTOF, systematic studies on its sensitivity to
489 different species, distinguishing the organic and inorganic contribution to the same peak in the spectra, and investigating peak
490 ratios are still required.

491 **Data availability**

492 The reference spectra are available upon request from the authors and will be made available in electronic format via the
493 EUROCHAMP-2020 data base (www.eurochamp.org).

494 **Author contributions**

495 X.S. characterised the LAAPTOF, measured all the particles samples, did the data analysis, produced all figures, and wrote the
496 manuscript. R.R. helped to characterise the LAAPTOF and to measure some of the particle samples. C.M. provided technical and
497 scientific support for characterising the LAAPTOF as well as data analysis, and for interpretation and discussion of the results.
498 WH provided scientific support for interpretation and discussion of the results. T.L. gave general advices and comments for this
499 paper. H.S. provided technical and scientific support for characterising the LAAPTOF, as well as suggestions for the data
500 analysis, interpretation and discussion. All authors contributed to the final text.

501 **Competing interests**

502 The authors declare that they have no conflicts of interest.

503 **Acknowledgements**

504 The authors gratefully thank the AIDA staff at KIT for helpful discussions and technical support, and the China Scholarship
505 Council (CSC) for financial support of Xiaoli Shen and Wei Huang. Special thanks go to Thea Schiebel, Kristina Höhler, and
506 Ottmar Möhler for discussions about the soil dust samples, to Isabelle Steinke for discussions regarding the plant samples, to
507 Robert Wagner for comments on the sea salt samples, to Konrad Kandler for providing the Morocco desert dust samples, to Roger
508 Funk and Thomas Hill for providing the soil dust samples, to Elena Gorokhova and Matt Salter for providing the sea salt with
509 *skeletonema marinoi* culture, and to Aeromegt GmbH for discussions about the LAAPTOF performance and analysis software.



510 **References**

511 Ackerman, A. A., Adam, J. A., Cairns, B., Cho, H., Gritsevich, M., Jethva, H., Kacenelenbogen, M., Kandler, K., Knobelspiesse,
512 K., Lanconelli, C., Lupi, A., Mazzola, M., Nousiainen, T., Peltoniemi, J. I., Platnick, S., Puttonen, E., Savenkov, S. N., Segal-
513 Rosenheimer, M., Sharma, S., Tomasi, C., Torres, O., and Zhang, Z.: Light scattering reviews 9: Light scattering and radiative
514 transfer, Springer-Praxis, 2015.

515 Ahern, A. T., Subramanian, R., Saliba, G., Lipsky, E. M., Donahue, N. M., and Sullivan, R. C.: Effect of secondary organic
516 aerosol coating thickness on the real-time detection and characterization of biomass-burning soot by two particle mass
517 spectrometers, *Atmos Meas Tech*, 9, 6117–6137, 2016.

518 Arndt, J., Sciare, J., Mallet, M., Roberts, G. C., Marchand, N., Sartelet, K., Sellegri, K., Dulac, F., Healy, R. M., and Wenger, J.
519 C.: Sources and mixing state of summertime background aerosol in the northwestern Mediterranean basin, *Atmos Chem Phys*, 17,
520 6975–7001, 2016.

521 Bohren, C. F. and Huffman, R. D.: Absorption and scattering of light by small particles, WILEY-VCH Verlag GmbH & Co.
522 KGaA, 2007.

523 Brands, M., Kamphus, M., Böttger, T., Schneider, J., Drewnick, F., Roth, A., Curtius, J., Voigt, C., Borbon, A., Beekmann, M.,
524 Bourdon, A., Perrin, T., and Borrmann, S.: Characterization of a newly developed aircraft-based laser ablation aerosol mass
525 spectrometer (ALABAMA) and first field deployment in urban pollution plumes over Paris during MEGAPOLI 2009, *Aerosol*
526 *Sci Tech*, 45, 46–64, 2011.

527 Burkholder, J. B., Abbatt, J. P. D., Barnes, I., Roberts, J. M., Melamed, M. L., Ammann, M., Bertram, A. K., Cappa, C. D.,
528 Carlton, A. G., Carpenter, L. J., Crowley, J. N., Dubowski, Y., George, C., Heard, D. E., Herrmann, H., Keutsch, F. N., Kroll, J.
529 H., McNeill, V. F., Ng, N. L., Nizkorodov, S. A., Orlando, J. J., Percival, C. J., Picquet-Varrault, B., Rudich, Y., Seakins, P. W.,
530 Surratt, J. D., Tanimoto, H., Thornton, J. A., Tong, Z., S., T. G., Wahner, A., Weschler, C. J., Wilson, K. R., and Ziemann, P. J.:
531 The essential role for laboratory studies in atmospheric chemistry, *Environ Sci Technol*, 51, 2519–2528, 2017.

532 Canagaratna, M. R., Jayne, J. T., Jimenez, J. L., Allan, J. D., Alfarra, M. R., Zhang, Q., Onasch, T. B., Drewnick, F., Coe, H.,
533 Middlebrook, A., Delia, A., Williams, L. R., Trimborn, A. M., Northway, M. J., DeCarlo, P. F., Kolb, C. E., Davidovits, P., and
534 Worsnop, D. R.: Chemical and microphysical characterization of ambient aerosols with the aerodyne aerosol mass spectrometer,
535 *Mass Spectrom Rev*, 26, 185–222, 2007.

536 Dall'Osto, M., Beddows, D. C. S., McGillicuddy, E. J., Esser-Gietl, J. K., Harrison, R. M., and Wenger, J. C.: On the
537 simultaneous deployment of two single-particle mass spectrometers at an urban background and a roadside site during SAPUSS,
538 *Atmos Chem Phys*, 16, 9693–9710, 2016.

539 Erdmann, N., Dell'Acqua, A., Cavalli, P., Gruning, C., Omenetto, N., Putaud, J. P., Raes, F., and Van Dingenen, R.: Instrument
540 characterization and first application of the single particle analysis and sizing system (SPASS) for atmospheric aerosols, *Aerosol*
541 *Sci Tech*, 39, 377–393, 2005.



- 542 Ervens, B., Feingold, G., Frost, G. J., and Kreidenweis, S. M.: A modeling study of aqueous production of dicarboxylic acids: 1.
543 Chemical pathways and speciated organic mass production, *J Geophys Res-Atmos*, 109, 2004.
- 544 Gaie-Levrel, F., Perrier, S., Perraudin, E., Stoll, C., Grand, N., and Schwell, M.: Development and characterization of a single
545 particle laser ablation mass spectrometer (SPLAM) for organic aerosol studies, *Atmos Meas Tech*, 5, 225–241, 2012.
- 546 Gard, E., Mayer, J. E., Morrical, B. D., Dienes, T., Ferguson, D. P., and Prather, K. A.: Real-time analysis of individual
547 atmospheric aerosol particles: Design and performance of a portable ATOFMS, *Anal Chem*, 69, 4083–4091, 1997.
- 548 Gemayel, R., Hellebust, S., Temime-Roussel, B., Hayeck, N., Van Elteren, J. T., Wortham, H., and Gligorovski, S.: The
549 performance and the characterization of laser ablation aerosol particle time-of-flight mass spectrometry (LAAP-ToF-MS), *Atmos*
550 *Meas Tech*, 9, 1947–1959, 2016.
- 551 Gross, D. S., Gälli, M. E., Silva, P. J., and Prather, K. A.: Relative sensitivity factors for alkali metal and ammonium cations in
552 single particle aerosol time-of-flight mass spectra, *Anal Chem*, 72, 416–422, 2000.
- 553 Hagemann, R., Corsmeier, U., Kottmeier, C., Rinke, R., Wieser, A., and Vogel, B.: Spatial variability of particle number
554 concentrations and NO_x in the Karlsruhe (Germany) area obtained with the mobile laboratory 'AERO-TRAM', *Atmos Environ*,
555 94, 341–352, 2014.
- 556 Hinz, K. P., Greweling, M., Drews, F., and Spengler, B.: Data processing in on-line laser mass spectrometry of inorganic,
557 organic, or biological airborne particles, *J Am Soc Mass Spectr*, 10, 648–660, 1999.
- 558 Jimenez, J. L., Canagaratna, M. R., Donahue, N. M., Prevot, A. S. H., Zhang, Q., Kroll, J. H., DeCarlo, P. F., Allan, J. D., Coe,
559 H., Ng, N. L., Aiken, A. C., Docherty, K. S., Ulbrich, I. M., Grieshop, A. P., Robinson, A. L., Duplissy, J., Smith, J. D., Wilson,
560 K. R., Lanz, V. A., Hueglin, C., Sun, Y. L., Tian, J., Laaksonen, A., Raatikainen, T., Rautiainen, J., Vaattovaara, P., Ehn, M.,
561 Kulmala, M., Tomlinson, J. M., Collins, D. R., Cubison, M. J., Dunlea, E. J., Huffman, J. A., Onasch, T. B., Alfarra, M. R.,
562 Williams, P. I., Bower, K., Kondo, Y., Schneider, J., Drewnick, F., Borrmann, S., Weimer, S., Demerjian, K., Salcedo, D.,
563 Cottrell, L., Griffin, R., Takami, A., Miyoshi, T., Hatakeyama, S., Shimono, A., Sun, J. Y., Zhang, Y. M., Dzepina, K., Kimmel,
564 J. R., Sueper, D., Jayne, J. T., Herndon, S. C., Trimborn, A. M., Williams, L. R., Wood, E. C., Middlebrook, A. M., Kolb, C. E.,
565 Baltensperger, U., and Worsnop, D. R.: Evolution of organic aerosols in the atmosphere, *Science*, 326, 1525–1529, 2009.
- 566 Johnston, M. V.: Sampling and analysis of individual particles by aerosol mass spectrometry, *J Mass Spectrom*, 35, 585–595,
567 2000.
- 568 Kamphus, M., Ettner-Mahl, M., Brands, M., Curtius, J., Drewnick, F., and Borrmann, S.: Comparison of two aerodynamic lenses
569 as an inlet for a single particle laser ablation mass spectrometer, *Aerosol Sci Tech*, 42, 970–980, 2008.
- 570 Kulkarni, P., Baron, P. A., and Willeke, K.: *Aerosol measurement: Principles, techniques, and applications*, John Wiley & Sons,
571 Inc., 2011.



- 572 Li, W., Sun, J., Xu, L., Shi, Z., Riemer, N., Sun, Y., Fu, P., Zhang, J., Lin, Y., Wang, X., Shao, L., Chen, J., Zhang, X., Wang, Z.,
573 and Wang, W.: A conceptual framework for mixing structures in individual aerosol particles, *J Geophys Res-Atmos*, 121,
574 13784–13798, 2016.
- 575 Liu, P., Ziemann, P. J., Kittelson, D. B., and McMurry, P. H.: Generating Particle Beams of Controlled Dimensions and
576 Divergence .2. Experimental Evaluation of Particle Motion in Aerodynamic Lenses and Nozzle Expansions, *Aerosol Sci Tech*,
577 22, 314–324, 1995.
- 578 Marsden, N., Flynn, M. J., Allan, J. D., and Coe, H.: On-line differentiation of mineral phase in aerosol particles by ion formation
579 mechanism using a LAAP-TOF single particle mass spectrometer, *Atmos Meas Tech Discuss*, doi: 10.5194/amt-2017-85, 2017.
- 580 Marsden, N., Flynn, M. J., Taylor, J. W., Allan, J. D., and Coe, H.: Evaluating the influence of laser wavelength and detection
581 stage geometry on optical detection efficiency in a single-particle mass spectrometer, *Atmos Meas Tech*, 9, 6051–6068, 2016.
- 582 Moffet, R. C., de Foy, B., Molina, L. T., Molina, M. J., and Prather, K. A.: Measurement of ambient aerosols in northern Mexico
583 City by single particle mass spectrometry, *Atmos Chem Phys*, 8, 4499–4516, 2008.
- 584 Murphy, D. M.: The design of single particle laser mass spectrometers, *Mass Spectrom Rev*, 26, 150–165, 2007.
- 585 Murphy, D. M., Cziczo, D. J., Froyd, K. D., Hudson, P. K., Matthew, B. M., Middlebrook, A. M., Peltier, R. E., Sullivan, A.,
586 Thomson, D. S., and Weber, R. J.: Single-particle mass spectrometry of tropospheric aerosol particles, *J Geophys Res-Atmos*,
587 111, 2006.
- 588 Murphy, D. M., Middlebrook, A. M., and Warshawsky, M.: Cluster analysis of data from the Particle Analysis by Laser Mass
589 Spectrometry (PALMS) instrument, *Aerosol Sci Tech*, 37, 382–391, 2003.
- 590 Murphy, D. M. and Thomson, D. S.: Laser ionization mass-spectroscopy of single aerosol-particles, *Aerosol Sci Tech*, 22, 237–
591 249, 1995.
- 592 Noble, C. A. and Prather, K. A.: Real-time single particle mass spectrometry: a historical review of a quarter century of the
593 chemical analysis of aerosols, *Mass Spectrom Rev*, 19, 248–274, 2000.
- 594 Pöschl, U.: Atmospheric aerosols: Composition, transformation, climate and health effects, *Angew Chem Int Edit*, 44, 7520–
595 7540, 2005.
- 596 Pratt, K. A. and Prather, K. A.: Mass spectrometry of atmospheric aerosols-Recent developments and applications. Part II: On-
597 line mass spectrometry techniques, *Mass Spectrom Rev*, 31, 17–48, 2012.
- 598 Ramisetty, R., Abdelmonem, A., Shen, X., Saathoff, H., Mohr, C., and Leisner, T.: Comparison of nanosecond and femtosecond
599 laser ablation in single particle mass spectrometer for atmospheric applications, *Atmos Meas Tech Discuss*, doi.org/10.5194/amt-
600 2017-357, 2017.



- 601 Reitz, P., Zorn, S. R., Trimborn, S. H., and Trimborn, A. M.: A new, powerful technique to analyze single particle aerosol mass
602 spectra using a combination of OPTICS and the fuzzy c-means algorithm, *J Aerosol Sci*, 98, 1–14, 2016.
- 603 Roth, A., Schneider, J., Klimach, T., Mertes, S., van Pinxteren, D., Herrmann, H., and Borrmann, S.: Aerosol properties, source
604 identification, and cloud processing in orographic clouds measured by single particle mass spectrometry on a central European
605 mountain site during HCCT-2010, *Atmos Chem Phys*, 16, 505–524, 2016.
- 606 Saathoff, H., Möhler, O., Schurath, U., Kamm, S., Dippel, B., and Mihelcic, D.: The AIDA soot aerosol characterisation
607 campaign 1999, *J Aerosol Sci*, 34, 1277–1296, 2003.
- 608 Saathoff, H., Naumann, K. H., Möhler, O., Jonsson, A. M., Hallquist, M., Kiendler-Scharr, A., Mentel, T. F., Tillmann, R., and
609 Schurath, U.: Temperature dependence of yields of secondary organic aerosols from the ozonolysis of α -pinene and limonene,
610 *Atmos Chem Phys*, 9, 1551–1577, 2009.
- 611 Schill, G. P. and Tolbert, M. A.: Heterogeneous ice nucleation on phase-separated organic-sulfate particles: effect of liquid vs.
612 glassy coatings, *Atmos Chem Phys*, 13, 4681–4695, 2013.
- 613 Schmidt, S., Schneider, J., Klimach, T., Mertes, S., Schenk, L. P., Curtius, J., and Borrmann, S.: Online single particle analysis
614 of ice particle residuals from mountain-top mixed-phase clouds using laboratory derived particle type assignment, *Atmos Chem*
615 *Phys*, 17, 575–594, 2017.
- 616 Schreiner, J., Schild, U., Voigt, C., and Mauersberger, K.: Focusing of aerosols into a particle beam at pressures from 10 to 150
617 Torr, *Aerosol Sci Tech*, 31, 373–382, 1999.
- 618 Seinfeld, J. H. and Pandis, S. N.: *Atmospheric chemistry and physics: From air pollution to climate change*, Wiley, J & Sons,
619 Inc., Hoboken, New Jersey, 2006.
- 620 Silva, P. J., Carlin, R. A., and Prather, K. A.: Single particle analysis of suspended soil dust from Southern California, *Atmos*
621 *Environ*, 34, 1811–1820, 2000.
- 622 Su, Y. X., Sipin, M. F., Furutani, H., and Prather, K. A.: Development and characterization of an aerosol time-of-flight mass
623 spectrometer with increased detection efficiency, *Anal Chem*, 76, 712–719, 2004.
- 624 Trimborn, A., Hinz, K.-P., and Spengler, B.: Online analysis of atmospheric particles with a transportable laser mass
625 spectrometer, *Aerosol Sci Tech*, 33, 191–201, 2000.
- 626 Tsigaridis, K., Krol, M., Dentener, F. J., Balkanski, Y., Lathière, J., Metzger, S., Hauglustaine, D. A., and Kanakidou, M.:
627 Change in global aerosol composition since preindustrial times, *Atmos Chem Phys*, 6, 5143–5162, 2006.
- 628 Usher, C. R., Michel, A. E., and Grassian, V. H.: Reactions on mineral dust, *Chem Rev*, 103, 4883–4939, 2003.
- 629 Wagner, R., Kaufmann, J., Möhler, O., Saathoff, H., Schnaiter, M., Ullrich, R., and Leisner, T.: Heterogeneous ice nucleation
630 ability of NaCl and sea salt aerosol particles at cirrus temperatures, *J. Geophys. Res. (Atmos.)* (in preparation), 2017.



- 631 Williams, L. R., Gonzalez, L. A., Peck, J., Trimborn, D., McInnis, J., Farrar, M. R., Moore, K. D., Jayne, J. T., Robinson, W. A.,
632 Lewis, D. K., Onasch, T. B., Canagaratna, M. R., Trimborn, A., Timko, M. T., Magoon, G., Deng, R., Tang, D., Blanco, E. D. L.
633 R., Prévôt, A. S. H., Smith, K. A., and Worsnop, D. R.: Characterization of an aerodynamic lens for transmitting particles greater
634 than 1 micrometer in diameter into the Aerodyne aerosol mass spectrometer, *Atmos Meas Tech*, 6, 3271–3280, 2013.
- 635 Yu, J. Z., Cocker, D. R., Griffin, R. J., Flagan, R. C., and Seinfeld, J. H.: Gas-phase ozone oxidation of monoterpenes: Gaseous
636 and particulate products, *J. Atmos. Chem.*, 34, 207–258, 1999.
- 637 Zawadowicz, M. A., Abdelmonem, A., Mohr, C., Saathoff, H., Froyd, K. D., Murphy, D. M., Leisner, T., and Cziczo, D. J.:
638 Single-particle time-of-flight mass spectrometry utilizing a femtosecond desorption and ionization laser, *Anal Chem*, 87, 12221–
639 12229, 2015.
- 640 Zawadowicz, M. A., Lance, S., Jayne, J. T., Croteau, P., Worsnop, D. R., Mahrt, F., Leisner, T., and Cziczo, D. J.: Quantifying
641 and improving the performance of the Laser Ablation Aerosol Particle Time of Flight Mass Spectrometer (LAAPToF)
642 instrument, *Atmos Meas Tech Discuss*, doi: 10.5194/amt-2017-1, 2017.
- 643 Zelenyuk, A., Cai, Y., and Imre, D.: From agglomerates of spheres to irregularly shaped particles: Determination of dynamic
644 shape factors from measurements of mobility and vacuum aerodynamic diameters, *Aerosol Sci Tech*, 40, 197–217, 2006a.
- 645 Zelenyuk, A. and Imre, D.: Single particle laser ablation time-of-flight mass spectrometer: An introduction to SPLAT, *Aerosol*
646 *Sci Tech*, 39, 554–568, 2005.
- 647 Zelenyuk, A., Imre, D., Cai, Y., Mueller, K., Han, Y. P., and Imrich, P.: SpectraMiner, an interactive data mining and
648 visualization software for single particle mass spectroscopy: A laboratory test case, *Int J Mass Spectrom*, 258, 58–73, 2006b.
- 649 Zelenyuk, A., Yang, J., Choi, E., and Imre, D.: SPLAT II: An aircraft compatible, ultra-sensitive, high precision instrument for
650 in-situ characterization of the size and composition of fine and ultrafine particles, *Aerosol Sci Tech*, 43, 411–424, 2009.
- 651 Zhang, Q., Jimenez, J. L., Canagaratna, M. R., Allan, J. D., Coe, H., Ulbrich, I., Alfarra, M. R., Takami, A., Middlebrook, A. M.,
652 Sun, Y. L., Dzepina, K., Dunlea, E., Docherty, K., DeCarlo, P. F., Salcedo, D., Onasch, T., Jayne, J. T., Miyoshi, T., Shimono,
653 A., Hatakeyama, S., Takegawa, N., Kondo, Y., Schneider, J., Drewnick, F., Borrmann, S., Weimer, S., Demerjian, K., Williams,
654 P., Bower, K., Bahreini, R., Cottrell, L., Griffin, R. J., Rautiainen, J., Sun, J. Y., Zhang, Y. M., and Worsnop, D. R.: Ubiquity
655 and dominance of oxygenated species in organic aerosols in anthropogenically-influenced Northern Hemisphere midlatitudes,
656 *Geophys Res Lett*, 34, 2007.
- 657 Zhao, W. X., Hopke, P. K., and Prather, K. A.: Comparison of two cluster analysis methods using single particle mass spectra,
658 *Atmos Environ*, 42, 881–892, 2008.
- 659

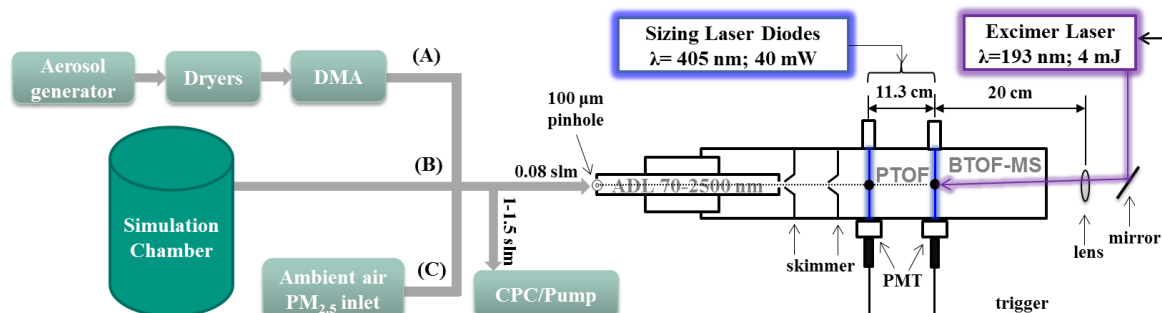
660 **Table 1: Summary of mass spectral patterns**

Species	Signature peaks in positive spectra	Signature peaks in negative spectra	Typical Peak Ratios histogram x_0 (width)*
potassium	39 K ⁺ , 41 K ⁺		(I39+I40):I41= \sim 13.5(0.9)
calcium	40 Ca ⁺ , 56 CaO ⁺		
aluminium	27 Al ⁺	43 AlO ⁻ , 59 AlO ₂ ⁻	
silicon	28 Si ⁺ , 44 SiO ⁺	60 SiO ₂ ⁻ , 76 SiO ₃ ⁻ , 77 HSiO ₃ ⁻	(I76+I77):I60= \sim 1.0 (0.33)
silicon & aluminium	27 Al ⁺ , 28 Si ⁺ , 44 SiO ⁺	43 AlO ⁻ , 59 AlO ₂ ⁻ , 60 SiO ₂ ⁻ , 76 SiO ₃ ⁻ , 77 HSiO ₃ ⁻ , 119 AlSiO ₄ ⁻ , 179 AlSiO ₄ .SiO ₂ ⁻	
ammonium	18 NH ₄ /H ₂ O ⁺ , 30 NO ⁺		
nitrate	30 NO ⁺	46 NO ₂ ⁻ , 62 NO ₃ ⁻	
sulphate		32 S ⁻ , 48 SO ⁻ , 64 SO ₂ ⁻ , 80 SO ₃ ⁻ , 81HSO ₃ ⁻ , 96 SO ₄ ⁻ , 97 HSO ₄ ⁻	
chloride		35 Cl ⁻ , 37 Cl ⁻	(I35+I36):I37= \sim 3.2(0.9)
elemental carbon	12 _n C _n ⁺	12 _n C _n ⁻	
organics		24 C ₂ ⁻ , 25 C ₂ H ⁻ , 26 C ₂ H ₂ /CN ⁻	
organic acids		45 COOH ⁻ , 59 CH ₂ COOH ⁻ , 71 CCH ₂ COOH ⁻ , 73 C ₂ H ₄ COOH ⁻ , 85 C ₃ H ₄ COOH ⁻ , 99 C ₄ H ₆ COOH ⁻ , 117 (CO) ₃ OOH ⁻	
nitrogen-containing organics		26 CN ⁻ , 42 CNO ⁻	
unsaturated organics		25 C ₂ H ⁻ , 26 C ₂ H ₂ ⁻ unknown fragments 49- and 73-	
aromatic compounds	77 C ₆ H ₅ ⁺ , 91C ₇ H ₇ ⁺ , 103 C ₈ H ₇ ⁺ /105 C ₈ H ₉ ⁺ , 115 C ₉ H ₇ ⁺	25 C ₂ H ⁻ , 26 C ₂ H ₂ ⁻ unknown fragments 49- and 73-	

661

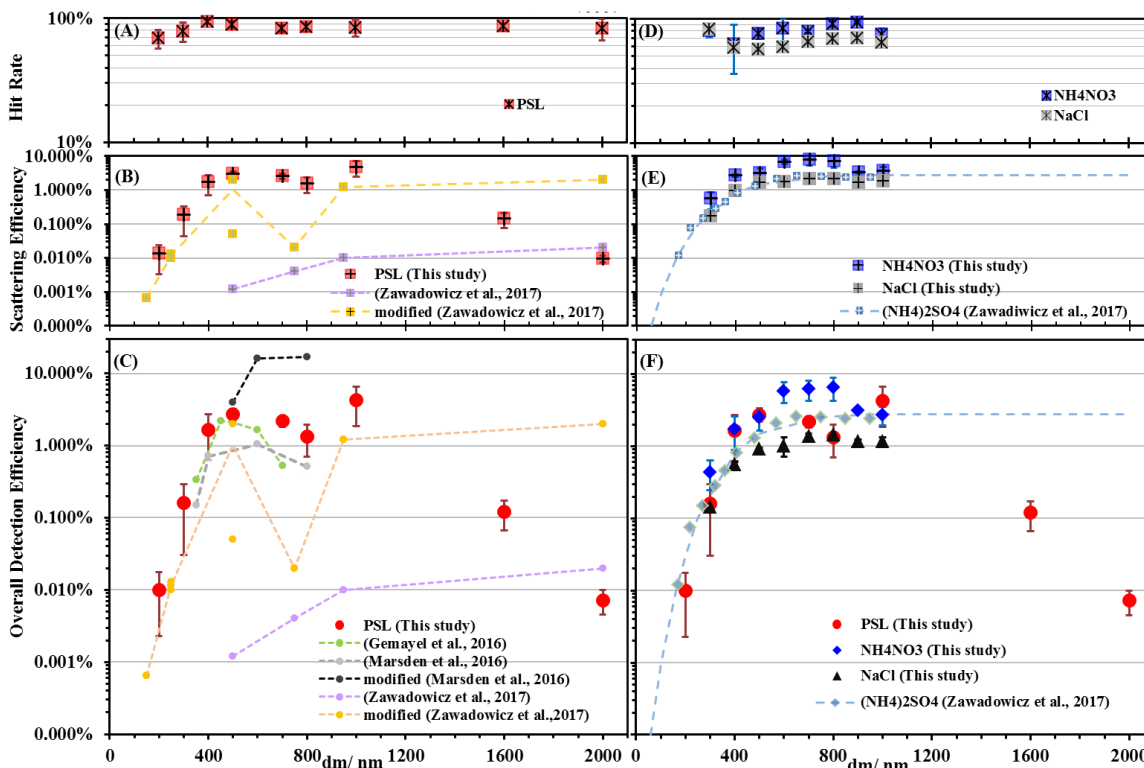
662 Note:

663 *We have made histograms for the three typical peak ratios, respectively (ref. Fig. S3). Histogram x_0 is the expected value that indicates the
 664 position of the peak resulting from Gaussian fit, and the width is the corresponding standard deviation. I is short for the intensity of the
 665 corresponding peak in LAAPTOF spectra; typical peak ratios for potassium and chloride are based on pure and mixed salt that containing K
 666 and Cl; typical peak ratios for silicon are based on pure SiO₂.



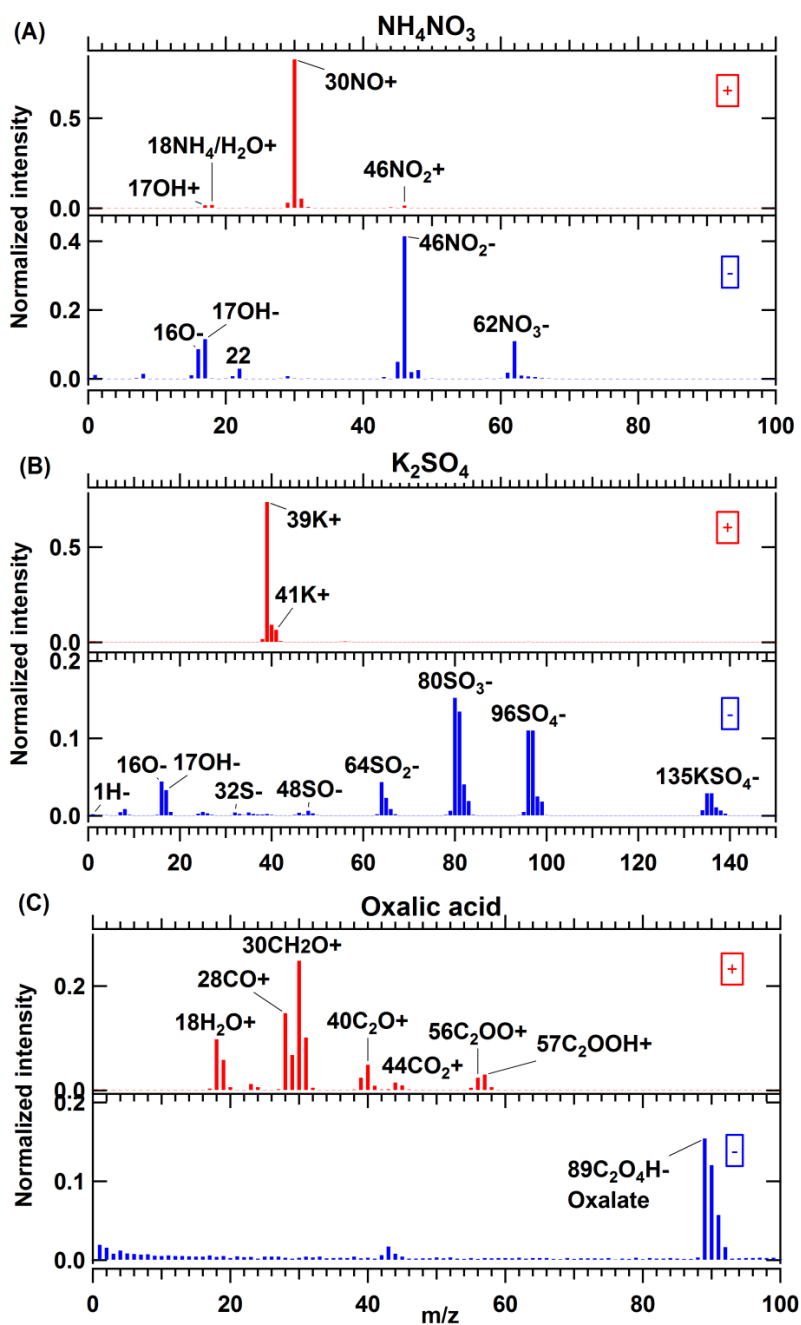
667

668 Figure 1: Schematic of the LAAPTOF instrument and three different experimental setups for measuring standard samples: setup (A)
 669 e.g. PSL, NH₄NO₃ and K₂SO₄ particles, were generated from a nebulizer, passed through two dryers, size-selected by a differential
 670 mobility analyzer (DMA), and then measured by LAAPTOF; setup (B) was used for samples generated in or dispersed into the AIDA
 671 chamber (~84.5 m³) or samples dispersed into a stainless steel cylinder (~0.18 m³); setup (C) was used for measuring ambient aerosols
 672 in field campaigns. In addition, some particles, e.g. mineral dust, were sampled directly from the headspace of their reservoirs.



673

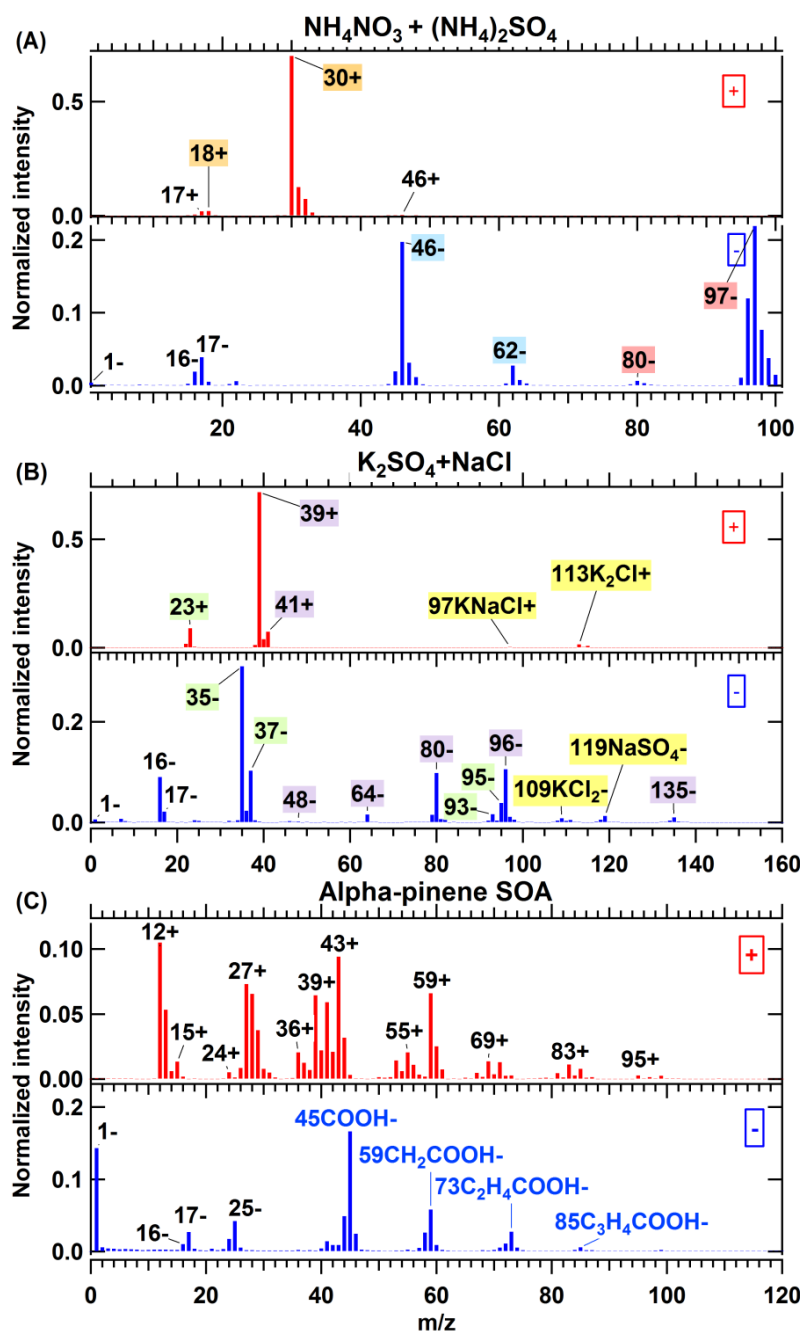
674 Figure 2: Hit rate (HR, panel A and D), scattering efficiency (SE, panel B and E), and overall detection efficiency (ODE, panel C and
 675 F) for PSL, ammonium nitrate (NH₄NO₃) and sodium chloride (NaCl) salt particles as a function of mobility diameter, d_m . Aerosol
 676 particles in this study were generated from a nebulizer and size-selected by DMA. In panel (B) and (E), optical counting efficiencies
 677 (OCE) for PSL and ammonium sulphate ((NH₄)₂SO₄) at the detection beam from the study by Zawadowicz et al. (2017), corresponding
 678 to the SE defined in this study, are plotted for comparison. In panel (C) and (F), ODE for PSL and salt particles from other studies
 679 (Gemayel et al., 2016; Marsden et al., 2016; Zawadowicz et al., 2017) are plotted for comparison. In this figure, dashed lines are used
 680 only for guiding the eyes.



681

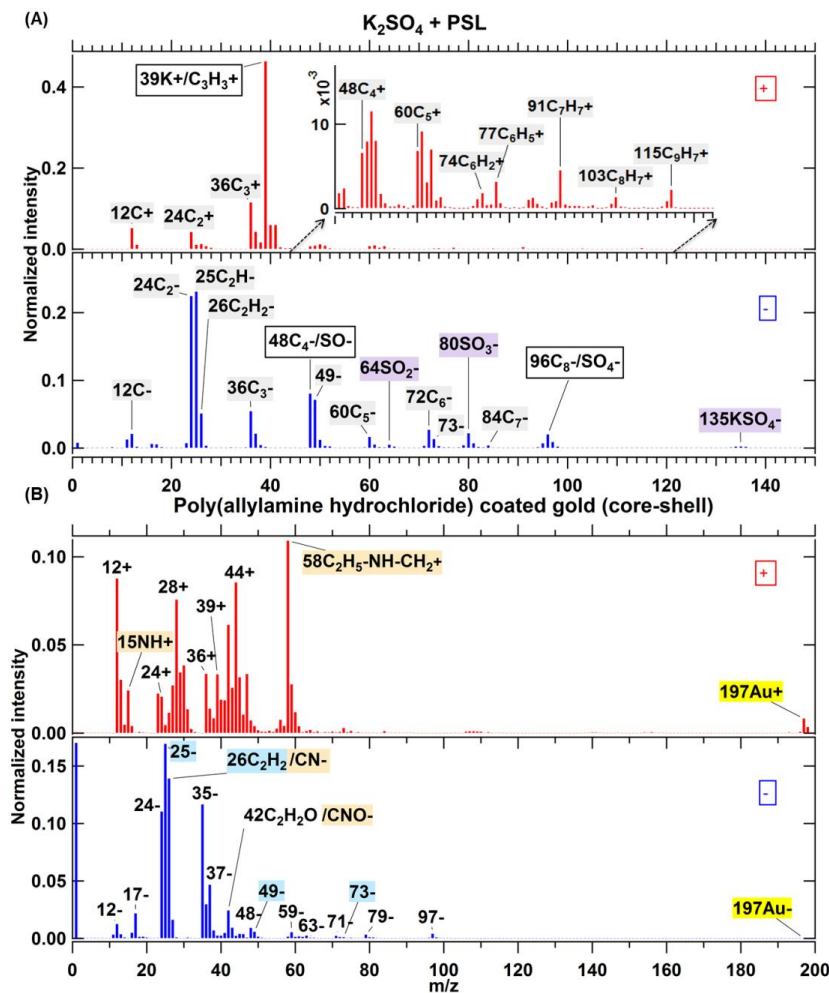
682 Figure 3: Average mass spectra for pure compound aerosol particles: (A) NH_4NO_3 (dva=1160 nm), 497 single spectra averaged, (B)

683 K_2SO_4 (dva=1465 nm), 300 single spectra averaged, and (C) oxalic acid particles (dva=1081 nm), 736 single spectra averaged.



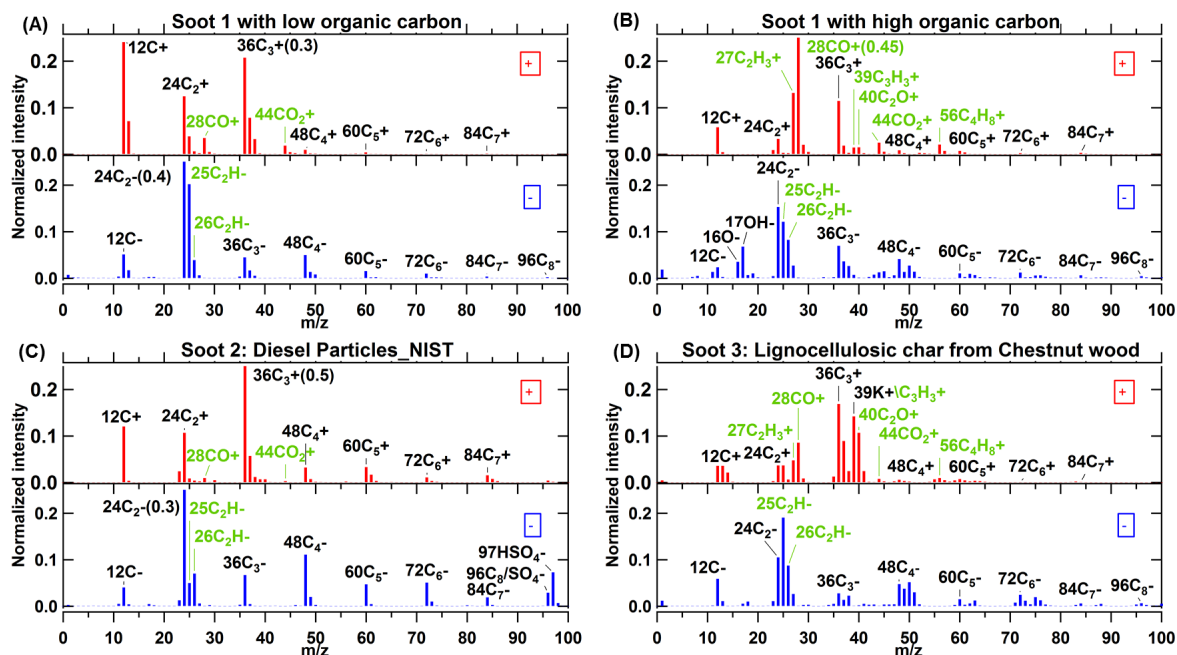
684

685 Figure 4: Average mass spectra for particles of internal mixtures of (A) NH_4NO_3 and $(\text{NH}_4)_2\text{SO}_4$, 454 single spectra
 686 averaged and (B) NaCl and K_2SO_4 , 259 single spectra averaged as well and (C) secondary organic aerosol (SOA)
 687 particles from α -pinene ozonolysis, which was performed in the APC chamber, then the resulting particles were transferred into the
 688 AIDA chamber at 263 K and 95% RH, $d_{\text{va}} = 505$ nm, 1938 single spectra averaged. In panel (A), red, blue and orange labels represent
 689 fragments of sulphate, nitrate and ammonium, respectively. In panel (B), green and purple labels represent fragments from NaCl and
 690 K_2SO_4 components (see section 3.2.1) in the mixed particles, respectively; yellow labels represent the fragments only in the internal
 691 mixture of NaCl and K_2SO_4 . In panel (C), labels with blue text represent fragments of organic acids.



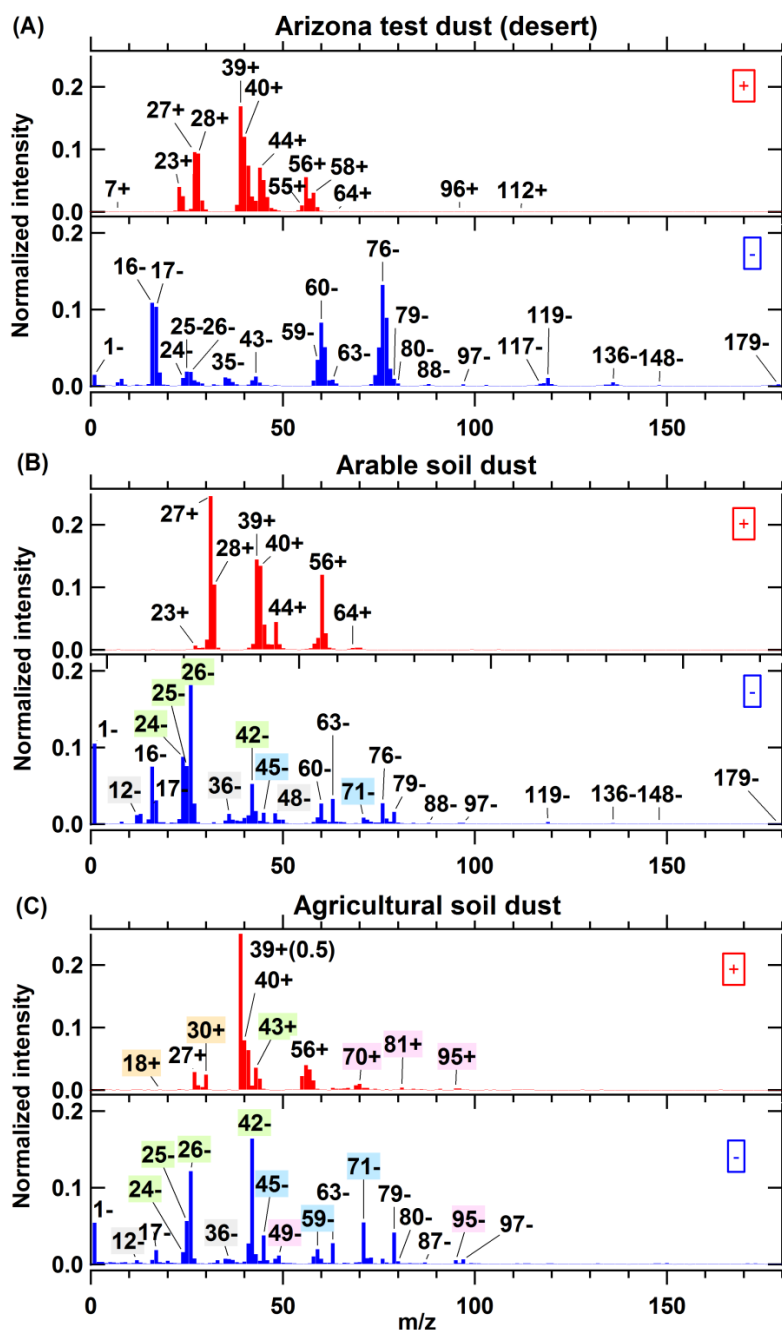
692

693 Figure 5: Average mass spectra for core-shell particles of (A) PSL coated with K_2SO_4 , $d_{va} = 805$ nm, 609 single spectra averaged, and
 694 (B) poly(allylamine hydrochloride) coated gold (Au) particles with geometric 300 nm gold core and 50 nm thick organic shell, 417
 695 single spectra averaged. In panel (A), grey and purple labels represent the fragments arising from pure PSL and pure K_2SO_4
 696 components, respectively; box labels represent the fragments with contributions from core and shell compounds. In panel (B) orange
 697 and blue labels represent the fragments arising from nitrogen-containing and unsaturated organic compounds, respectively, and
 698 yellow labels represent gold.



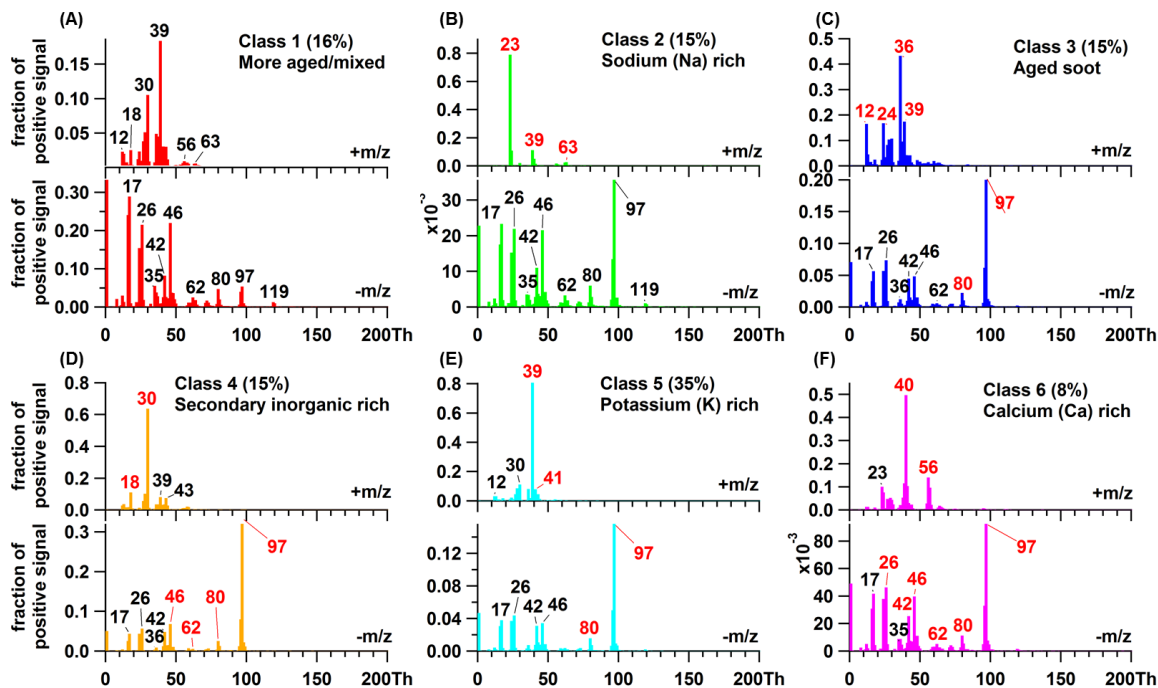
699

700 Figure 6: Average mass spectra for soot particles with (A) high elemental carbon (EC), low organic carbon (OC) content and (B) low
 701 EC and high OC from combustion of propane in a soot generator and transferred to a stainless steel cylinder of ~ 0.2 m³ volume, as well
 702 as soot particles of (C) diesel particles (NIST) and (D) lignocellulosic char from Chestnut wood. In panel (A) and (C), the numbers in
 703 brackets beside peak 36⁺ and 24⁻ are the exact intensity values for them. The OC signatures are labeled in green. The numbers of
 704 spectra averaged for each spectrum are 617 (A), 347 (B), 533 (C) and 390 (D).



705

706 Figure 7: Average mass spectra for particles of complex mixtures: (A) Arizona test dust (desert dust), directly sampled into the
 707 LAAPTOF from a shaken bottle (B) arable soil dust, collected from Gottesgabe in Germany, was dispersed by a rotating brush
 708 generator and injected via cyclones into the AIDA chamber at 256 K and 80% RH, and (C) agricultural soil dust, collected from
 709 harvesting machines after rye and wheat harvest, were generated by using the same method as (B). For panel (B) and (C), fragments
 710 labelled in green represent more intensive organic signatures in soil dust particles; grey labels represent EC patterns; blue labels
 711 represent organic acids; orange labels represent ammonium salts; red labels represent unknown fragments. The numbers of spectra
 712 averaged for each spectrum are 261 (A), 583 (B), and 286 (C).



713

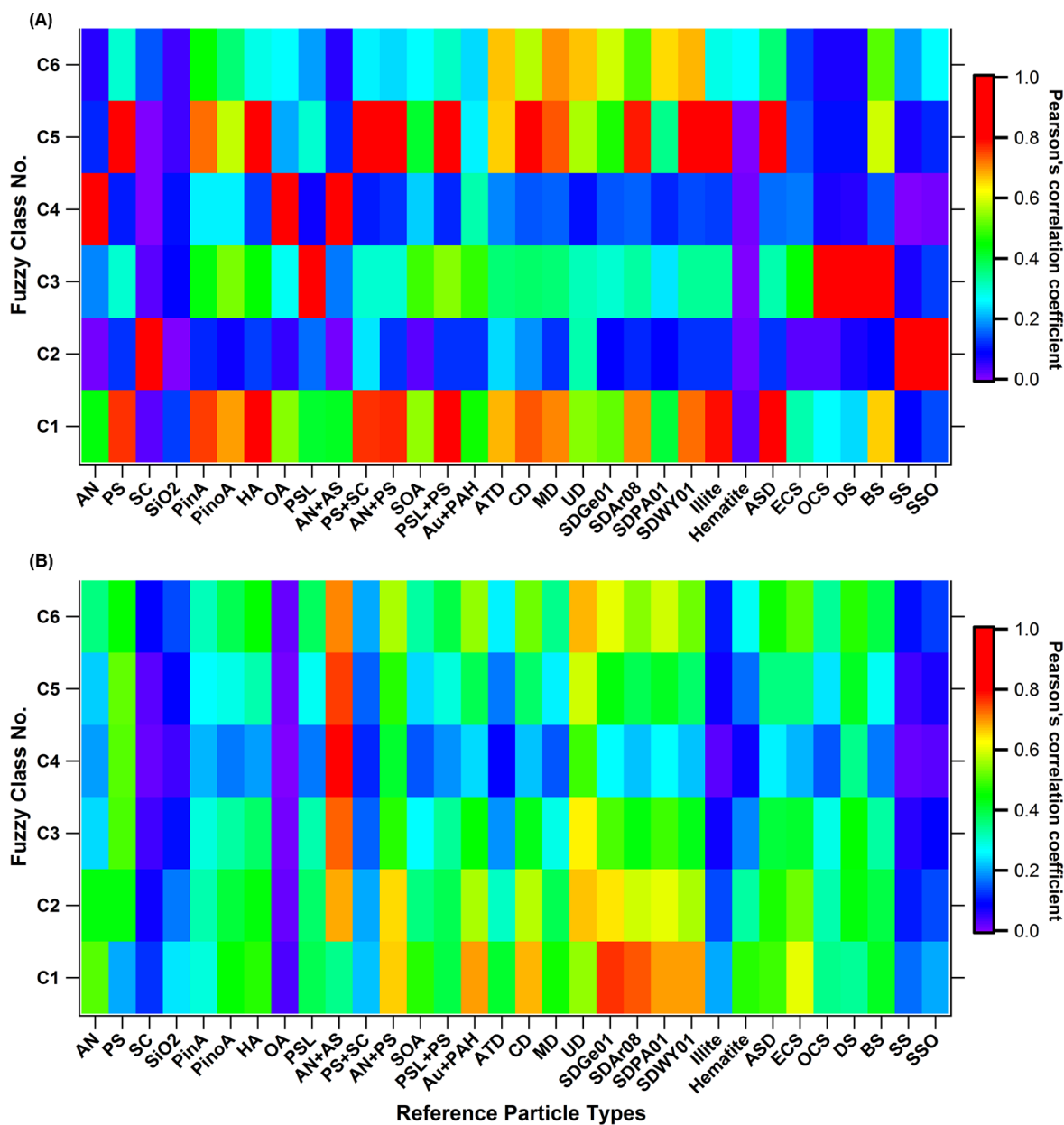
714

715

716

717

Figure 8: Mass spectra for six classes of particles measured on July 29th, 2016 during the field campaign TRAM01, based on classification according to Fuzzy c-means algorithm. The percentage in each pair of spectra (A to F) gives us information about the similarity of the total aerosols to different classes. The red tags represent the signatures for each typical class, but there is no red tag in spectra B, since this class is more aged particles that containing signatures for different classes. Mean particle size: $d_{va} (676 \pm 165)$ nm.



718

719 Figure 9: Correlation between Fuzzy classification results (6 classes, C1 to C6) and laboratory-based reference spectra. Panel (A) and
 720 (B) are the correlation results for the positive and negative spectra, respectively. AN is short for ammonium nitrate, PS-potassium
 721 sulphate, SC-sodium chloride, Pina-pinic acid, Pino-pinonic acid, HA-humid acid, OA-oxalic acid, ATD-Arizona test dust, CD-Cairo
 722 dust, MD-Morocco dust, UD-urban dust, SDGe01 and SDPA01-soil dusts sampled at two sites from Germany, SDAr08- soil dust from
 723 Argentina, SDWY01-soil dust from Wyoming in USA, ASD-agricultural soil dust, ECS-EC rich soot1, OCS-OC rich soot1, DS- diesel
 724 soot, BS- biomass burning soot, which is the lignocellulosic char from Chestnut wood, SS-pure sea salt, SSO-sea salt with organics.

